iScience

CellPress
OPEN ACCESS

Article

Ultrastructural maturation of the endbulb of Held active zones comparing wild-type and otoferlin-deficient mice

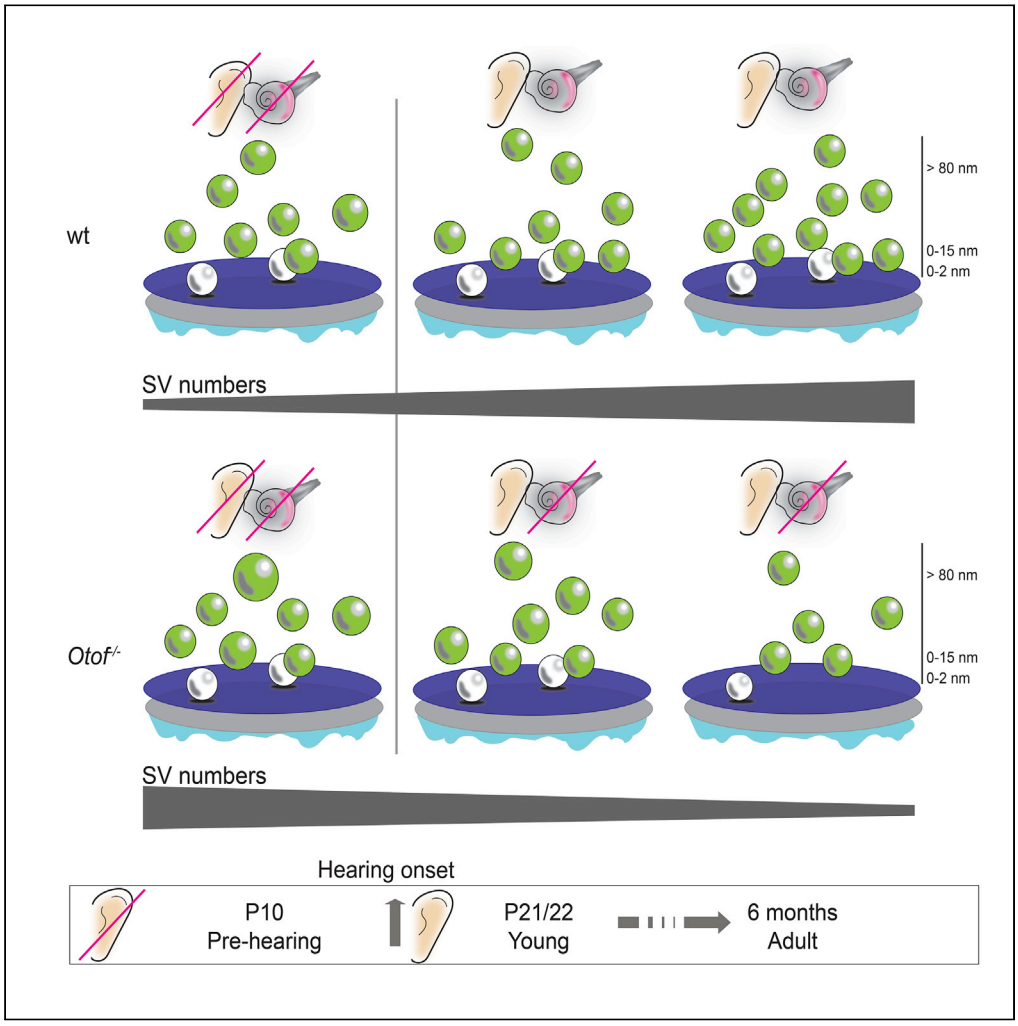

Anika Hintze, Mehmet Gültas, Esther A. Semmelhack, Carolin Wichmann

carolin.wichmann@med.uni-goettingen.de

Highlights

Maturation of wt endbulb of Held active zones leads to more synaptic vesicles

At endbulbs of otoferlin knockout mice, synaptic vesicles decline with age

Mainly two distinct synaptic vesicle populations are affected

Synaptic vesicles sizes are reduced in six-month-old otoferlin knockout animals

Hintze et al., iScience 24, 102282
April 23, 2021
https://doi.org/10.1016/j.isci.2021.102282

iScience

CellPress
OPEN ACCESS

Article

Ultrastructural maturation of the endbulb of Held active zones comparing wild-type and otoferlin-deficient mice

Anika Hintze,[1,2,3] Mehmet Gültas,[4] Esther A. Semmelhack,[5] and Carolin Wichmann[1,2,6,*]

SUMMARY

Endbulbs of Held are located in the anteroventral cochlear nucleus and present the first central synapses of the auditory pathway. During development, endbulbs mature functionally to enable rapid and powerful synaptic transmission with high temporal precision. This process is accompanied by morphological changes of endbulb terminals. Loss of the hair cell-specific protein otoferlin (Otof) abolishes neurotransmission in the cochlea and results in the smaller endbulb of Held terminals. Thus, peripheral hearing impairment likely also leads to alterations in the morphological synaptic vesicle (SV) pool size at individual endbulb of Held active zones (AZs). Here, we investigated endbulb AZs in pre-hearing, young, and adult wild-type and *Otof*$^{-/-}$ mice. During maturation, SV numbers at endbulb AZs increased in wild-type mice but were found to be reduced in *Otof*$^{-/-}$ mice. The SV population at a distance of 0–15 nm was most strongly affected. Finally, overall SV diameters decreased in *Otof*$^{-/-}$ animals during maturation.

INTRODUCTION

The mammalian auditory system encodes acoustic stimuli with exquisitely high temporal precision (Moser et al., 2006; Safieddine and Wenthold, 1999; Wang et al., 2011). Various processes such as directional sound localization as well as interindividual communication essentially rely on this fidelity (Ashida and Carr, 2011; Eddins et al., 2018; Grothe et al., 2010).

In mammals, the conversion of a physical sound wave into neural code is mediated via ribbon synapses between cochlear inner hair cells (IHCs) and primary afferent spiral ganglion neurons (Moser et al., 2006). Here, type I afferent auditory nerve fibers (ANFs) (Liberman and Oliver, 1984) project into the cochlear nucleus (CN) as a first central relay station (Nicol and Walmsley, 2002; Ryugo and Fekete, 1982). Consequently, auditory synaptopathy at IHC ribbon synapses leads to functional impairments downstream on CN level (Moser and Starr, 2016). For example, the proper function of exocytosis at IHC ribbon synapses relies on the hair-cell-specific C_2 domain protein otoferlin (Otof) (Pangrsic et al., 2010; Roux et al., 2006). In humans, mutations in *OTOF* cause recessive, non-syndromic hearing impairment DFNB9 (Rodríguez-Ballesteros et al., 2008; Varga et al., 2006; Yasunaga et al., 1999). Likewise, genetic deletion of *Otof* (*Otof*$^{-/-}$) in mice abolishes exocytosis at IHC ribbon synapses. Therefore, the peripheral auditory pathway fails to transduce acoustic input and auditory brain stem responses are absent in *Otof*$^{-/-}$ mice (Roux et al., 2006). This functional impairment has previously been shown to also affect CN structure (Wright et al., 2014).

Early reports noted that multipolar cells within the CN comprised morphologically and functionally distinct classes (Harrison & Irving, 1965, 1966; Lorente de Nó, 1981; Osen, 1969; Ostapoff et al., 1994). Specifically, in the anteroventral cochlear nucleus (AVCN), large presynaptic terminals are found that wrap around the cell body of two types of bushy cells (BCs). The primary task of this cell type is to encode precise timing information of the sound stimulus, which is ensured due to BCs' outstanding ability of phase locking (Joris et al., 1994; Paolini et al., 2001; Smith et al., 1993; Wang and Manis, 2006). Structural classifications of BCs into globular bushy cells (GBCs) and spherical bushy cells (SBCs) were mainly drawn based on data from cats (Brawer and Morest, 1975; Osen, 1969; Wu and Oertel, 1984). GBCs are innervated by smaller endings, which were termed as modified endbulbs (Rouiller et al., 1986) and project into the contralateral medial nucleus of the trapezoid body forming the calyx of Held (Ryugo and Spirou, 2009; Borst and Soria van

[1]Molecular Architecture of Synapses Group, Institute for Auditory Neuroscience, InnerEarLab and Center for Biostructural Imaging of Neurodegeneration, University Medical Center Göttingen, 37075 Göttingen, Germany

[2]Collaborative Research Center 1286, University of Göttingen, Göttingen, Germany

[3]Göttingen Graduate School for Neurosciences, Biophysics and Molecular Biosciences, University of Göttingen, Göttingen, Germany

[4]Breeding Informatics Group, Department of Animal Sciences, Georg-August-University Göttingen, Göttingen, Germany

[5]Developmental, Neural, and Behavioral Biology MSc/PhD Program, University of Göttingen, Göttingen, Germany

[6]Lead contact

*Correspondence: carolin.wichmann@med.uni-goettingen.de

https://doi.org/10.1016/j.isci.2021.102282

Hoeve, 2012; Joris and Trussell, 2018). SBCs are enveloped by the large endbulbs of Held, as it was found for different vertebrates including rodents (Ryugo and Spirou, 2009; Willard and Ryugo, 1983). They transmit the signal to the contralateral and ipsilateral medial superior olive and to the ipsilateral lateral superior olive (Cant and Casseday, 1986; Warr, 1966). In mice, it remains difficult to distinguish between SBCs and GBCs via their morphology. Rather, regional differences in the synaptic organization of ANF inputs to BCs have been reported (Lauer et al., 2013).

Endbulbs of Held develop from small entities to large finger-like terminals (Limb and Ryugo, 2000; Ryugo and Fekete, 1982; Ryugo and Spirou, 2009). At mature endbulbs, 500–2000 active zones (AZs) (Ryugo et al., 1996) contribute to the high reliability of signal transmission (Babalian et al., 2003; Brenowitz and Trussell, 2001; Nicol and Walmsley, 2002; Pfeiffer, 1966), which is characterized by highly synchronous release (Yang and Xu-Friedman, 2010). Before hearing onset, the auditory pathway exhibits stereotyped bursts of action potentials (Babola et al., 2018; Sonntag et al., 2009; Tritsch et al., 2010a, 2010b), which change to sensory-driven higher spiking rates combined with irregular spiking after hearing onset. Morphologically, endbulbs of Held AZs show presynaptic clusters of clear synaptic vesicles (SVs) and typically a curvature of the postsynaptic density (PSD) (Ryugo et al., 1997). For most synapse types, SVs are sorted in three functional pools: (i) the readily releasable pool (RRP) of SVs, (ii) the recycling pool, and (iii) the reserve pool (reviewed in [Rizzoli and Betz, 2005]). The RRP is widely believed to correspond to the fraction of morphologically docked SVs (Kaeser and Regehr, 2017; Schikorski and Stevens, 2001). Consequently, their number at the AZ determines synapse strength (Murthy et al., 2001; Schikorski and Stevens, 1999; Walmsley et al., 1998). Hence, the determination of ultrastructural SV pools can yield insight into mechanisms of synapse function. The advent of cryo-electron microscopic techniques allowed a novel view on the SV organization at presynaptic AZs. Using these powerful methods, SVs could be assigned to distinct populations based on not only their distance to the AZ membrane but also due to the complement of their filamentous connections i.e., molecular tethers — which play a major role determining SV distance to the AZ membrane (Cole et al., 2016; Fernández-Busnadiego et al., 2010, 2013; Landis et al., 1988; Siksou et al., 2007; Wesseling et al., 2019).

We hypothesize that long-term activity changes due to maturation or sensory deprivation induce alterations of the spatial arrangement and size of morphological SV pools at endbulb AZs. Precisely, (i) we expected that the number of SVs per AZ increases during development to support high transmission fidelity at mature AZs, also taking into account the transition from pre-hearing to hearing, which is accompanied by changes in activity patterns. After hearing onset, a larger amount of SVs might be required to reply to more diverse activity patterns. (ii) We further predict that in deaf *Otof*$^{-/-}$ mice the SV numbers at endbulb AZs might be reduced due to the functional impairment caused by the lack of exocytosis at IHC ribbon synapses. (iii) These potential changes in SV numbers might then be restricted to specific SV populations. Finally, (iv) SV diameters are expected to negatively correlate with activity levels as shown for the endbulb of Held upon monaural conductive hearing loss (Clarkson et al., 2016). Therefore, we employed high-pressure freezing (HPF) with subsequent freeze substitution (FS) of acutely prepared AVCN vibratome slices in order to preserve the tissue in a near-native state. We used electron tomography (ET) to investigate the AZs in 3D with the highest axial resolution as it has previously be done for other central synapse preparations (Cole et al., 2016; Imig et al., 2014; Maus et al., 2020; Siksou et al., 2007). This way, distances of SVs as well as the number of docked SVs could be determined unambiguously across the AZ. Hearing onset in mice occurs at the age of P11/12 (Mikaelian and Ruben, 1965). Thus, we chose three different age-groups, pre-hearing (P10), young post-hearing (P21/22), and adult mice (six months) to investigate structural hallmarks of endbulb synaptic maturation. We compared wild-type (wt) C57BL6/J endbulb of Held AZs with AZs of deaf *Otof*$^{-/-}$ mice, in which peripheral sound encoding is disrupted while central processing remains unaffected.

We found a steady increase of SV number per AZ in wt, but the average number of docked SVs did not change during maturation. Moreover, specific SV pools at a distance of 5–15 nm from the plasma membrane might contribute to reliable release at wt AZs. In contrast, the number of SVs per AZ strikingly declined in aging *Otof*$^{-/-}$ mice. In conclusion, upon a decrease of sound evoked activity, fewer SVs are available at the endbulb of Held presynaptic AZs.

RESULTS

Structural preservation of acutely sliced and cryo-preserved AVCNs

We performed HPF/FS followed by ET to determine the SV distances to the AZ membrane, applying the same categorization criteria as previous studies investigating other synapse types (Cole et al., 2016;

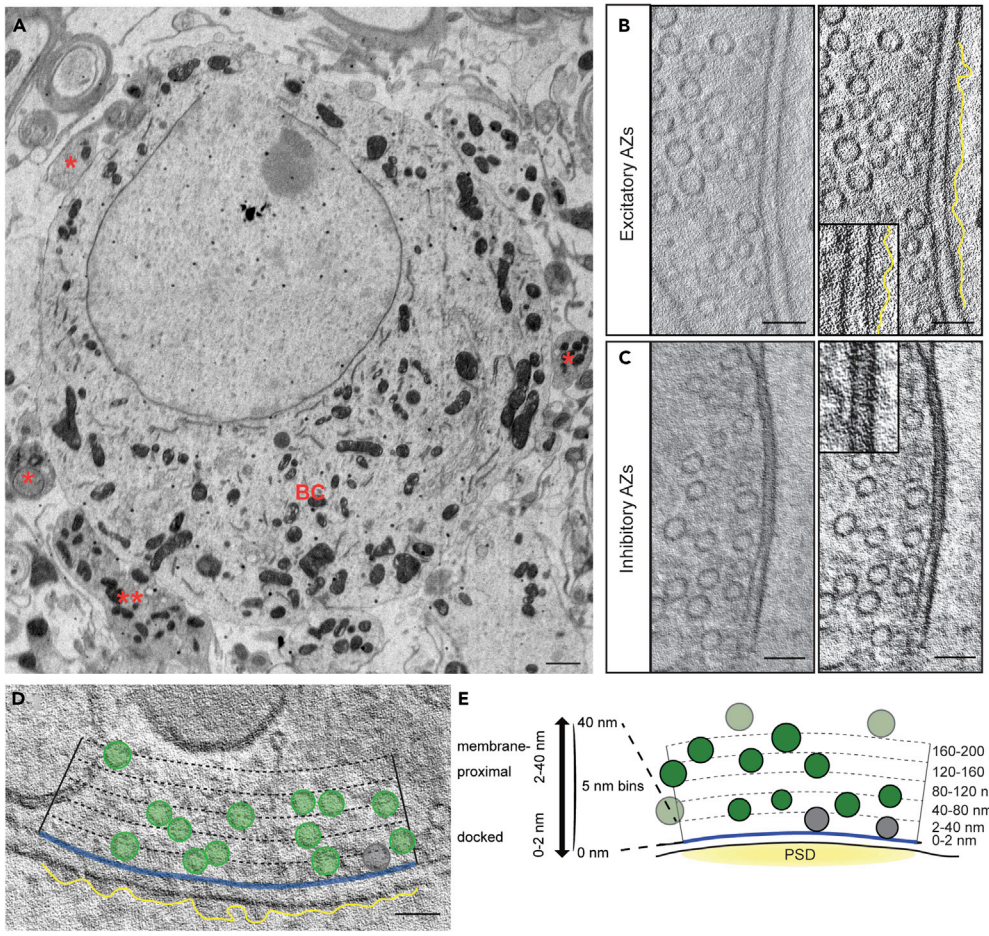

Figure 1. Morphological criteria used for AZ quantification

(A) Electron micrograph of a BC with several presynaptic contacts (*). The large terminal represents an endbulb of Held (**). Scale bar: 1 μm.

(B) Left: example virtual section of an excitatory AZ with a continuous - in HPF/FS samples fuzzy appearing - PSD that were included into the analysis, right: enhanced contrast of the same section, the rim of the PSD is highlighted (yellow line), see also inset.

(C) Left: virtual section of an asymmetrical contact, lacking the PSD, right: contrast enhanced same section as left, as also seen in the inset, a typical PSD is not present. These inhibitory AZs were excluded from the study after inspection of the whole tomogram.

(D and E) The criteria for including a tomogram into the analysis (presence of a PSD, presence of parallel pre- and postsynaptic membranes with a regular synaptic cleft) as well as for the SV quantification are shown on top of a virtual section (D) and in a scheme (E). All SVs (green) within a distance of 200 nm from the AZ membrane (blue) over the extent of the PSD (yellow) that was used to determine the AZ size were included in the analysis. SVs outside of this area (transparent green in [E]) were excluded. The shortest SV (outer leaflet)-AZ membrane distances were divided into 40-nm bins. The SVs from 2 to 40 nm were considered as membrane-proximal SVs. Additionally, from 0 to 40 nm, 5 nm steps were investigated. Morphologically docked SVs were considered separately and are depicted in gray. Scale bars in (B–D): 100 nm.

Fernández-Busnadiego et al., 2013; Imig et al., 2014; Maus et al., 2020). We focused on the excitatory endbulbs of Held, which harbor so-called asymmetric AZs (Gray, 1959), with a clear PSD (Figure 1B; García-Hernández et al., 2017; Nicol and Walmsley, 2002; O'Neil et al., 2011; Redd et al., 2000). Before subjected to quantification, all samples and tomograms underwent rigorous quality checks in order to determine the freezing quality. Next to the excitatory endbulbs, BCs also receive inhibitory input (Gómez-Nieto and Rubio, 2011; Keine and Rübsamen, 2015; Kuenzel, 2019; Lauer et al., 2013; Spirou et al., 2005). However, these presynaptic terminals are ultrastructurally distinguished from endbulbs as they are considerably smaller (Gulley and Reese, 1981; Spirou et al., 2005), and inhibitory synapses do not exhibit an elaborate PSD (Figure 1C; Colonnier, 1968; Harris and Weinberg, 2012; Tao et al., 2018) and are thus classified as

symmetrically synapses (Gray, 1959). Classically, inhibitory synapses have been described to contain flattened SVs (Lauer et al., 2013; Spirou et al., 2005; Tolbert and Morest, 1982). However, after rapid freezing and cryo-electron microscopy (Tao et al., 2018) or FS (Tatsuoka and Reese, 1989), SVs of inhibitory synapses remain spherical. Consequently, we had to thoroughly check for the presence or absence of a PSD to distinguish between excitatory and inhibitory AZs and excluded the latter tomograms from our analysis. Furthermore, only AZs from large terminals were considered, and the presence of parallel pre- and post-synaptic membranes with a regular synaptic cleft served as a required criterion to enable a reliable quantification of SV distances to the AZ membrane (Figure 1).

At wt AZs, the SV numbers increase during maturation

In this study, we set out to investigate (i) the changes of morphological SV pools at endbulb AZs during maturation from pre-hearing to adult stages and (ii) in response to auditory deprivation. Therefore, the morphological SV pools prior to hearing onset (P10), just after hearing onset (P21/22), and of adult (6 months [6M]) wt and *Otof*$^{-/-}$ mice were determined (Figure 2A).

In wt, the total SV number at a distance up to 200 nm from the plasma membrane increased slightly during maturation (Figure 2B; P10 with ~46 vs. ~64 at 6M; exact values and statistical details can be found in Table S1). Since tomograms were generated from 250-nm semithin sections, which typically do not include the whole AZ, we normalized the SV counts to the respective AZ area within each tomogram (Figure 2C). A significant increase of the SV numbers per μm^2 AZ area could be observed comparing P10 (~477 SVs/μm^2) and adult 6M wt endbulb AZs (~802 SVs/μm^2) (Figure 2D; Table S1).

Next, we determined the spatial distribution of SVs per area in membrane proximity, using 5-nm bin sizes from 0 to 40 nm (Figure 1E). We found an accumulation of SVs close to the membrane within 5–15 nm and more distant to the membrane above 80 nm. Interestingly, both fractions increased with advancing age at wt endbulb AZs (Figure 2E; values of the significant findings can be found in Table 1, all values see Table S1).

A decrease of SV numbers in aging *Otof*$^{-/-}$ mice

Endbulbs of Held AZs in congenitally deaf *Otof*$^{-/-}$ mice do not receive auditory input, which results in gross morphological changes of the endbulb terminals as described previously (Wright et al., 2014). In the current study, we report an increase of SV numbers at wt AZs during maturation. At *Otof*$^{-/-}$ endbulb AZs, the opposite trend becomes obvious. A significant decrease of the total SV counts and the SV numbers per μm^2 AZ area was detected when comparing young P22 to adult 6M mutant animals (Figures 2B and 2D; Table S2). However, closer inspection of different SV populations revealed an initial increase of SV numbers within 5–15 nm during the transition from P10 to P22, which declines significantly at 6M of age (Figure 2E; Table S2). Additionally, a significant reduction of SVs at a distance of 80–200 nm was observed in 6M *Otof*$^{-/-}$ mice compared to P22 *Otof*$^{-/-}$ AZs.

In a direct comparison to the corresponding wt controls, SV counts at 6M *Otof*$^{-/-}$ AZs were found to be significantly reduced — though being initially comparable at pre-hearing and early post-hearing stages (Tables S3–S5). This was also observed when normalizing the SV count to the AZ area (Figures 2D and 2E; Tables S3–S5; Table 1).

In order to visualize the overall SV organization, we employed quantification of 10-nm bins throughout 0–200 nm, which revealed for both genotypes that the SV density was high within 0–10 nm to the AZ membrane and decreased with distance. Comparable to the results presented above, upon aging, the number of SVs increased at wt AZs close to the membrane, while at *Otof*$^{-/-}$, an initial increase occurred from P10 to P22 AZs but a strong reduction was observed in adult mutant mice (Figure S1; Tables S6–S10).

In summary, developmental maturation of wt endbulbs of Held is accompanied by an increase in SV numbers at individual AZs. In deaf 6M old *Otof*$^{-/-}$ mice, a reduction of SVs was found. Both changes affected mainly two SV populations: (i) SVs at a distance of up to 15 nm to the AZ membrane and (ii) SVs that are located further away ($\geq$80 nm) (SV pool changes are schematized in Figure 3D; Tables S1–S5).

Decreasing proportion of docked SVs in membrane proximity at adult *Otof*$^{-/-}$ endbulb AZs

We distinguished in our analysis between two SV sub-populations, physically docked SVs (0–2 nm from the presynaptic AZ membrane) and membrane-proximal SVs (2–40 nm from the presynaptic AZ membrane,

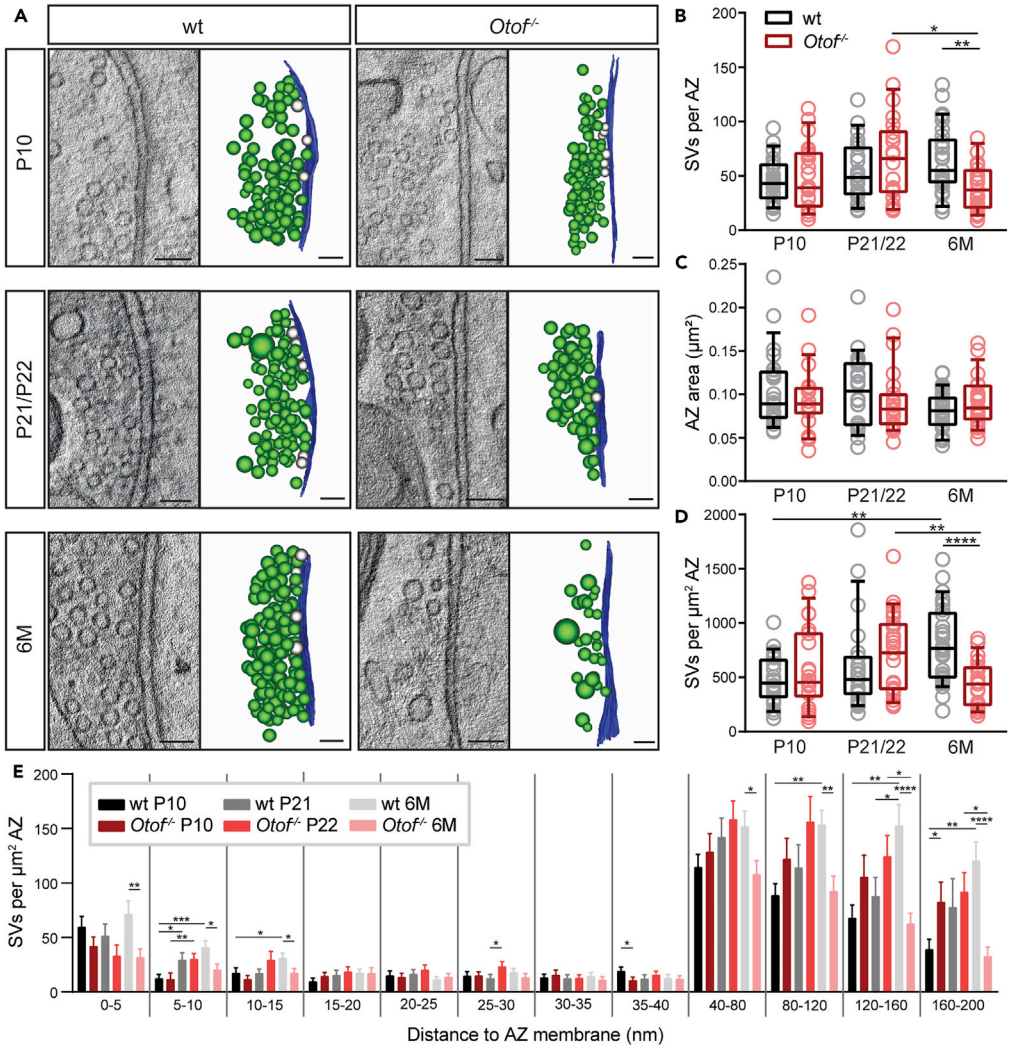

Figure 2. SV numbers of wt and *Otof*$^{-/-}$ endbulb AZs during maturation

(A) Single virtual sections and corresponding models of representative tomograms of AZs from P10, P21/22, and 6M wt and *Otof*$^{-/-}$ mice showing the AZ membrane (blue), SVs (green), and morphologically docked SVs (gray). Scale bars: 100 nm.

(B) Number of SVs within 200 nm of the AZ membrane. SV numbers are reduced in *Otof*$^{-/-}$ mice (wt 6M, 63.52 ± 5.63; *Otof*$^{-/-}$ 6M, 39.61 ± 4.68; **p = 0.0020 and *Otof*$^{-/-}$ P22, 66.64 ± 8.73; *Otof*$^{-/-}$ 6M, 39.61 ± 4.68; *p = 0.0163).

(C) AZ size determined by following the PSD extent in each tomogram.

(D) Number of SVs within 200 nm of the AZ membrane normalized to the AZ area, which is decreased at *Otof*$^{-/-}$ AZs (*Otof*$^{-/-}$ P22, 726.0 ± 76.14; *Otof*$^{-/-}$ 6M, 431.3 ± 46.38; **p = 0.0099; wt 6M, 801.5 ± 65.67; *Otof*$^{-/-}$ 6M, 431.3 ± 46.38; ****p < 0.0001).

(E) Number of SVs within bins of 5 and 40 nm from the AZ normalized to the AZ area, see also Table 1. Data are presented as box and whisker plots that indicate median, lower/upper quartiles, 10–90th percentiles (B–D), or as bar graph that represent mean ± SEM (E).

*p < 0.05; **p < 0.01; ***p < 0.001; ****p < 0.0001. wt P10 (*N* = 4; *n* = 24), *Otof*$^{-/-}$ P10 (*N* = 3; *n* = 22), wt P21 (*N* = 3; *n* = 22), *Otof*$^{-/-}$ P22 (*N* = 3; *n* = 23), wt 6M (*N* = 3; *n* = 29), and *Otof*$^{-/-}$ 6M (*N* = 3; *n* = 23), (*N*, number of animals; *n*, number of AZs). All values see Tables S1–S5.

docked SVs are excluded) — analogous to previous studies performing HPF/FS and subsequent ET (Imig et al., 2014; Maus et al., 2020; Watanabe et al., 2013). These definitions are based on different properties of the SVs, (i) physically docked SVs reduce upon stimulation, as demonstrated, for example, in experiments that combined optogenetic stimulations with rapid freezing and ET (Watanabe et al., 2013). Moreover, previous ET or cryo-ET studies on different synapse types identified a specific population of SVs, which are

Table 1. Significant differences in the distribution of SVs

	Distance to AZ membrane	wt P10	wt P21	wt 6M	p value
wt P10 vs. P21 vs. 6M	5-10 nm	13.00 ± 3.04 (9.17)	29.83 ± 6.18 (21.09)	41.31 ± 5.71 (39.50)	P10 vs. P21: *p = 0.0236 P10 vs. 6M: ***p = 0.0002
	10-15 nm	18.01 ± 4.17 (13.03)	17.70 ± 3.23 (16.37)	31.66 ± 3.85 (28.60)	P10 vs. 6M: *p = 0.0171
	80-120 nm	89.10 ± 10.28 (82.06)	114.6 ± 20.4 (82.79)	154.0 ± 12.56 (165.8)	P10 vs. 6M: **p = 0.0051
	120-160 nm	68.29 ± 11.34 (68.50)	88.30 ± 16.71 (69.24)	153.2 ± 18.75 (130.4)	P10 vs. 6M: **p = 0.0010 P21 vs. 6M: *p = 0.0181
	160-200 nm	39.61 ± 8.66 (27.61)	78.09 ± 25.73 (35.87)	120.9 ± 16.6 (98.5)	P10 vs. 6M: **p = 0.0010
		Otof$^{-/-}$ P10	*Otof*$^{-/-}$ P22	*Otof*$^{-/-}$ 6M	
Otof$^{-/-}$ P10 vs. P22 vs. 6M	120-160 nm	106.1 ± 19.4 (66.7)	124.9 ± 18.58 (109.0)	63.03 ± 8.99 (62.64)	P22 vs. 6M: *p = 0.0230
	160-200 nm	83.14 ± 17.60 (52.28)	92.32 ± 16.93 (62.86)	33.19 ± 8.12 (16.15)	P22 vs. 6M: *p = 0.0151
		wt 6M	*Otof*$^{-/-}$ 6M		
6M wt vs. *Otof*$^{-/-}$	0-5 nm	71.81 ± 11.68 (49.23)	32.30 ± 7.15 (21.43)		**p = 0.0036
	5-10 nm	41.31 ± 5.71 (39.50)	20.83 ± 4.82 (13.33)		*p = 0.0110
	10-15 nm	31.66 ± 3.85 (28.60)	18.02 ± 3.52 (14.96)		*p = 0.0117
	40-80 nm	152.3 ± 13.4 (145.3)	108.4 ± 12.08 (85.71)		*p = 0.0231
	80-120 nm	154.0 ± 12.56 (165.8)	92.95 ± 13.17 (77.47)		**p = 0.0016
	120-160 nm	153.2 ± 18.75 (130.4)	63.03 ± 8.99 (62.64)		****p < 0.0001
	160-200 nm	120.9 ± 16.6 (98.5)	33.19 ± 8.12 (16.15)		****p < 0.0001

The number of SVs within the respective bins is normalized to the AZ area. Data are presented as mean ± SEM (median in brackets). More details about statistics can be found in Tables S1, S2, and S5.

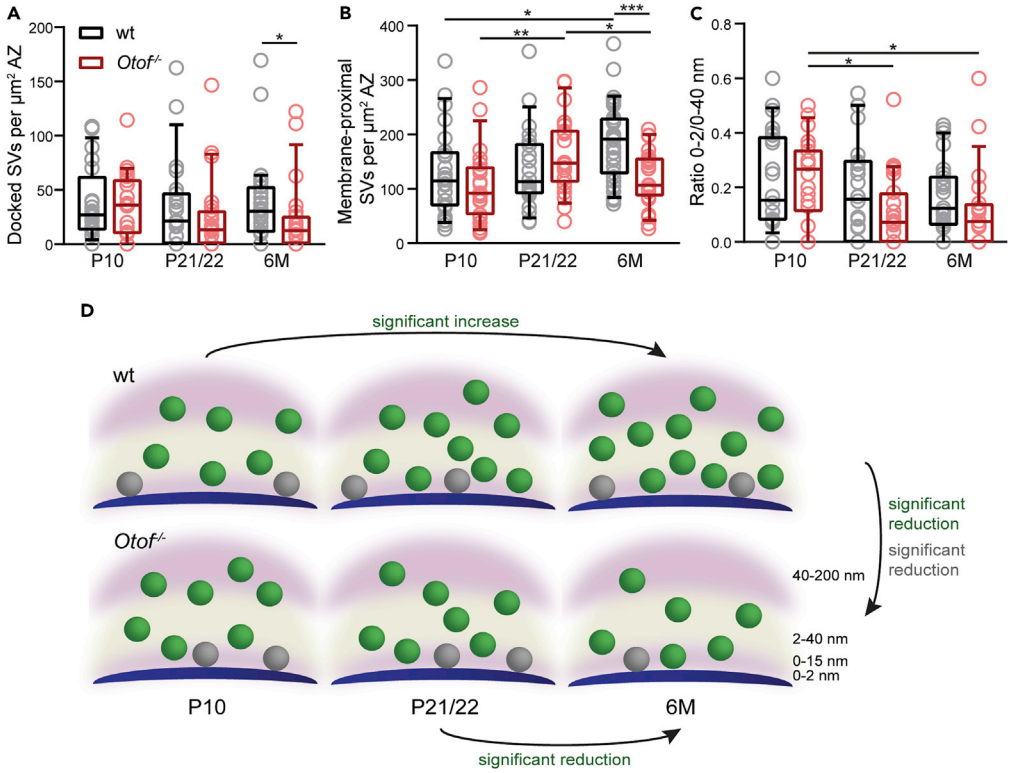

Figure 3. Docked and membrane-proximal SV at wt and *Otof*$^{-/-}$ AZs

(A) Number of morphologically docked SVs (0–2 nm from the AZ membrane) normalized to the AZ area.

(B) Number of SVs within 2–40 nm from the AZ membrane normalized to the AZ area.

(C) Proportion of docked SVs within all SVs from 0 to 40 nm distance. The ratio is smaller in 6M *Otof*$^{-/-}$ (*Otof*$^{-/-}$ P10, 0.2326 ± 0.0334; *Otof*$^{-/-}$ P22, 0.1102 ± 0.0276; *p = 0.0168; *Otof*$^{-/-}$ P10, 0.2326 ± 0.0334; *Otof*$^{-/-}$ 6M, 0.1203 ± 0.0304; *p = 0.0308). Data are presented as box and whisker plots that indicate median, lower/upper quartiles, 10–90th percentiles.

(D) Schematic summary of the SV pool changes. *p < 0.05; **p < 0.01; ***p < 0.001.

All values see Tables S1–S5.

connected via one single long tether of a maximum length of 45 nm to the AZ membrane (Cole et al., 2016; Fernández-Busnadiego et al., 2010, 2013; Siksou et al., 2007, 2009).

At wt endbulbs of Held, the number of docked SVs per µm^2 AZ area remained unaltered during maturation from pre-hearing to adult animals, while the number of membrane-proximal SVs steadily increased (Figures 3A and 3B). At *Otof*$^{-/-}$ AZs, the docked SV count was similar in all age-groups, but membrane-proximal SVs declined significantly at 6M of age (Figure 3B). Comparing both genotypes, significantly fewer docked SVs were observed at 6M *Otof*$^{-/-}$ endbulb AZs, which harbored on average ~22 docked SVs/µm^2 compared to ~37 in age-matched wt (Figure 3A). Finally, we analyzed the proportion of docked SVs relative to all SVs within 40 nm of the AZ membrane. This proportion decreased continuously upon maturation in both genotypes, which was statistically significant for *Otof*$^{-/-}$ P10 vs. 6M AZs, reducing from 0.23 to 0.12 (Figure 3C; Table S2).

The frequency distribution of docked SVs remained unaltered

Consistent with our observations, a previous study had already reported a highly variable number of docked SVs at endbulb AZs (Nicol and Walmsley, 2002). The total number of docked SVs per endbulb AZ was only reduced in *Otof*$^{-/-}$ 6M compared to wt 6M (Figure 4B), but their number ranged from 0 to 14 docked SVs at wt P10 AZs and from 0 to 16 at P22 *Otof*$^{-/-}$ AZs. However, most AZs of wt and *Otof*$^{-/-}$ endbulbs of all age-groups harbored 0–3 docked SVs (Figure 4D) as also shown in representative AZ top views of 3D models (Figure 4E). We analyzed the frequency distribution comparing maturation in wt and in

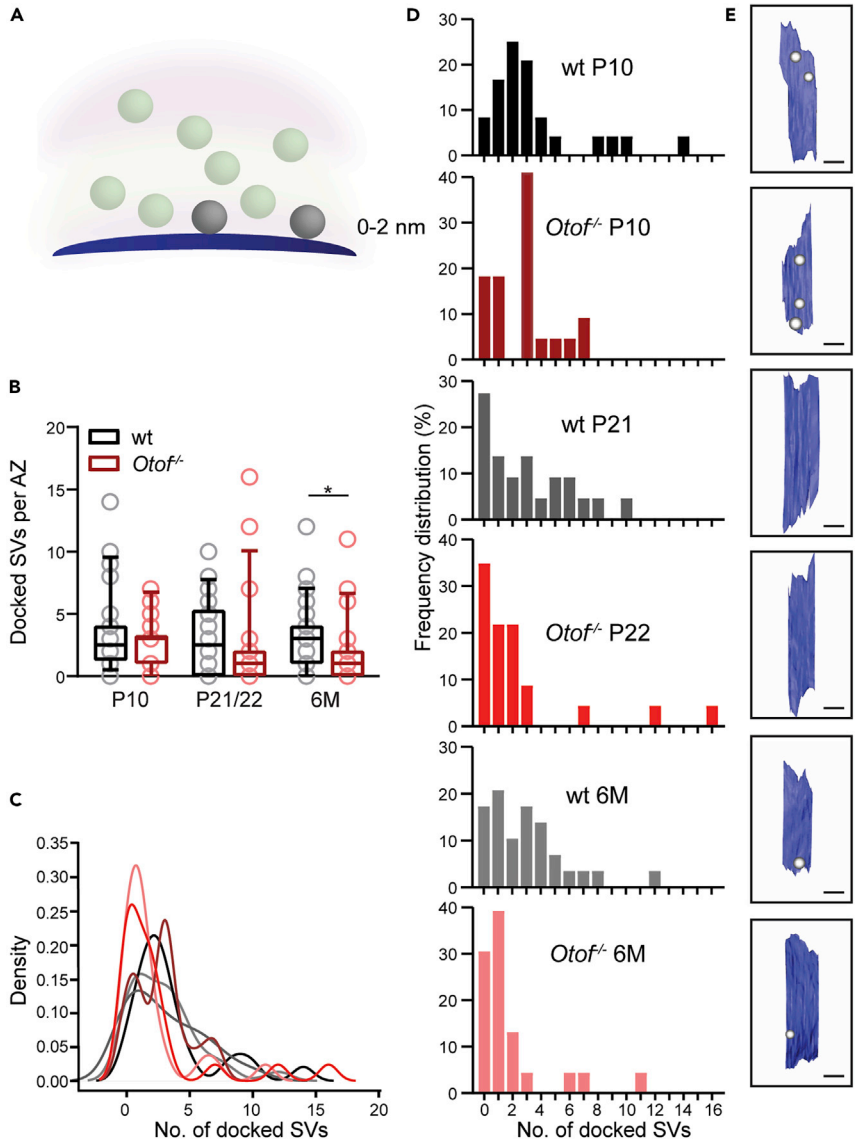

Figure 4. Frequency distribution of docked SVs

(A) Scheme of morphologically docked SVs (0–2 nm from the AZ membrane).

(B) Number of docked SVs per AZ. See also Tables S1–S5. The number of docked SVs is lower at 6M *Otof*$^{-/-}$ compared to 6M wt (wt 6M: 2.97 ± 0.51; *Otof*$^{-/-}$ 6M: 1.83 ± 0.56; *p = 0.0379). Data are presented as box and whisker plots that indicate median, lower/upper quartiles, 10–90th percentiles.

(C) Density distribution of the total number of docked SVs per AZ for all conditions.

(D) Histograms showing the relative frequency of AZs with 0–16 docked SVs at wt P10, P21, and 6M as well as at *Otof*$^{-/-}$ P10, P22, and 6M AZs.

(E) Top views of representative 3D models of AZ membranes with their most frequent number of docked SVs. Scale bars: 100 nm.

Otof$^{-/-}$ mice as well as between genotypes. The corresponding density and relative frequency distributions are depicted in Figures 4C and 4D, which were not significantly different (Table S11).

The number and distribution of membrane-proximal SVs remained largely unaffected

We next investigated the relative frequency distribution of the membrane-proximal SV pool (2–40 nm). At wt AZs, the membrane-proximal SV numbers remained unaltered at all ages and compared to *Otof*$^{-/-}$ AZs (Figure 5B). However, the difference between P10 *Otof*$^{-/-}$ AZs with ~9 membrane-proximal SVs in comparison to

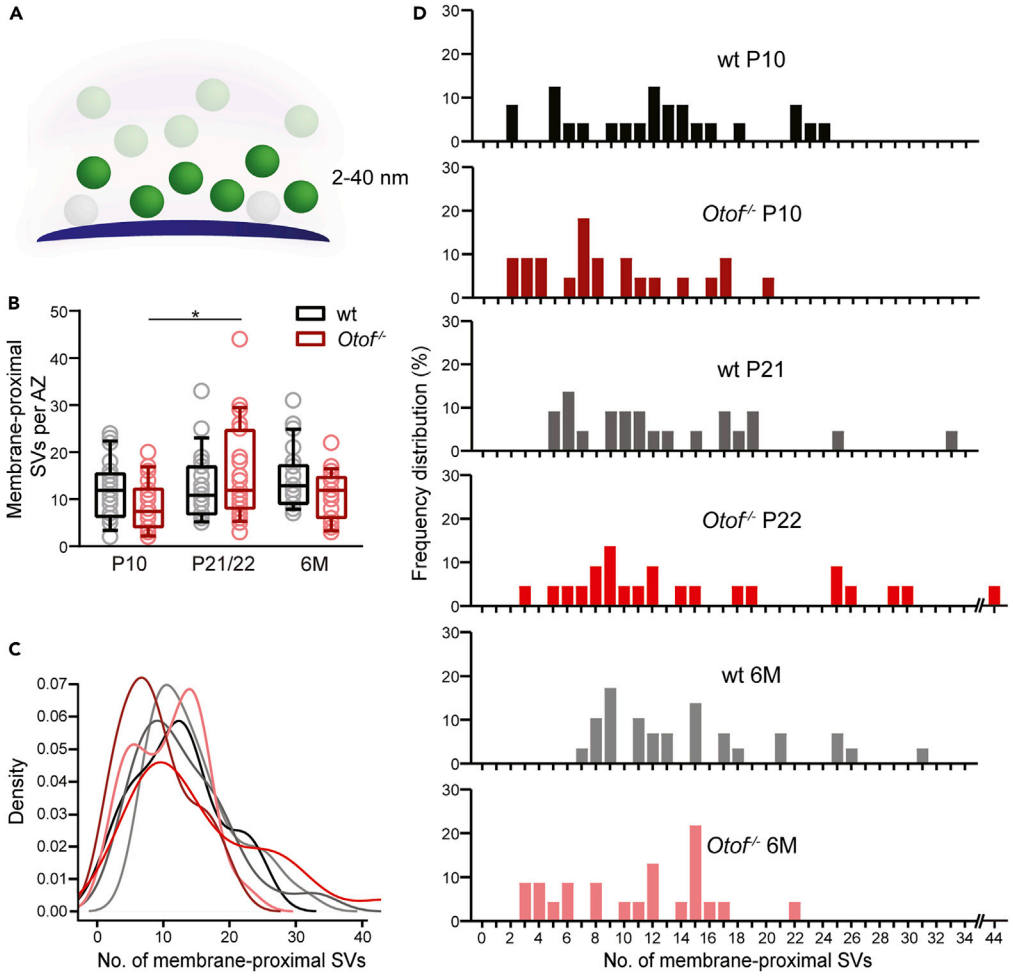

Figure 5. Frequency distribution of membrane-proximal SVs

(A) Scheme of membrane-proximal SVs (2–40 nm from the AZ membrane).

(B) Number of membrane-proximal SVs per AZ. Values see Tables S1–S5. Data are presented as box and whisker plots that indicate median, lower/upper quartiles, 10–90th percentiles. Membrane-proximal SVs increase at *Otof*$^{-/-}$ between P10 and P22 AZs (*Otof*$^{-/-}$ P10, 8.86 ± 1.13; *Otof*$^{-/-}$ P22, 15.39 ± 2.11; *p = 0.0104).

(C) Density distribution of the total number of membrane−proximal SVs per AZ for all conditions.

(D) Histograms showing the relative frequency of AZs with 0–44 SVs within 2–40 nm at wt and *Otof*$^{-/-}$ of all ages.

P22 AZs with ~15 SVs reached significance. The density and relative frequency distributions are shown in Figures 5C and 5D and the application of an *F*-test revealed a significantly broader distribution of membrane-proximal SVs in *Otof*$^{-/-}$ P22 compared to P10 and 6M (Table S11).

SV diameters are decreasing upon maturation at *Otof*$^{-/-}$ endbulb AZs

Acoustic deprivation was previously shown to decrease SV diameters at endbulbs of Held (Clarkson et al., 2016). Therefore, we compared the SV diameters in both genotypes and all age-groups (Figure 6, Tables S1–S5).

Indeed, in *Otof*$^{-/-}$ mice, the SV diameters decreased in the whole SV population from ~55 nm in P10 to ~50 nm at 6M of age (Figure 6A). A separate analysis of SV diameters of docked and membrane-proximal SVs revealed that this decrease appears in both populations (Figures 6C and 6E; Table S2). When comparing both genotypes, significantly larger SVs were found at *Otof*$^{-/-}$ P10 compared to age-matched wt. Again, this applies to all analyzed SV populations (Figures 6A, 6C, and 6E; Table S3). Finally, at 6M

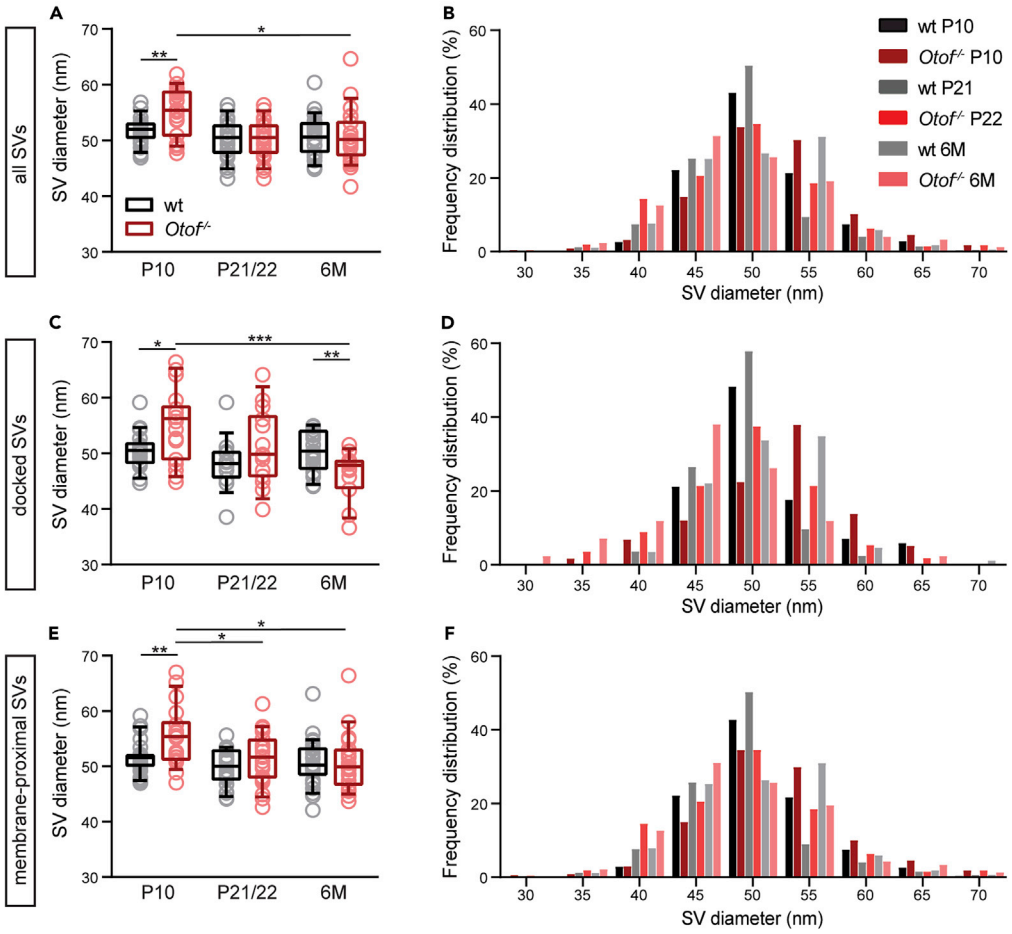

Figure 6. SV diameters change in *Otof*$^{-/-}$ endbulb AZs

(A, C, and E) Mean diameters averaged per tomogram for each condition. The mean diameters of all SVs decrease in *Otof*$^{-/-}$ mice (A, *Otof*$^{-/-}$ P10, 54.87 ± 0.90; *Otof*$^{-/-}$ 6M, 50.63 ± 1.03; *p = 0.0128), as well as of morphologically docked (C), and membrane-proximal (E) SVs per AZ. All values see Tables S1–S5. Data are presented as box and whisker plots that indicate median, lower/upper quartiles, 10–90th percentiles. *p < 0.05; **p < 0.01; ***p < 0.001. wt P10 (*N* = 4; *n* = 24), *Otof*$^{-/-}$ P10 (*N* = 3; *n* = 22), wt P21 (*N* = 3; *n* = 22), *Otof*$^{-/-}$ P22 (*N* = 3; *n* = 23), wt 6M (*N* = 3; *n* = 29), and *Otof*$^{-/-}$ 6M (*N* = 3; *n* = 23), (*N*, number of animals; *n*, number of AZs).

(B, D, and F) SV diameters were divided in 5 nm bins and the frequency distribution of SV diameters from all (B), morphologically docked (D), and membrane-proximal (F) SVs is shown as histograms.

Otof$^{-/-}$ endbulb AZs, docked SVs were found to be significantly smaller (~46 nm) compared to age-matched wt (~50 nm) (Figure 6C; Table S5). The frequency distributions of SV diameters are shown in Figures 6B, 6C, and 6F.

In summary, we found significant changes in SV numbers at wt and mutant endbulb of Held AZs that depend on the developmental stage. In wt, maturation resulted in an increase of SVs at endbulb AZs. This increase was not evenly distributed over the full quantified spatial range; instead, a prominent SV pool accumulated at 5–15 nm. Moreover, SVs further away (≥80 nm) to the membrane were also increased with age, indicating the presence of different morphological SV pools at endbulb AZs. The opposite trend was found at *Otof*$^{-/-}$ endbulbs, in that there was a reduction of SVs within 5–15 nm. In comparison to wt, the docked SV numbers decreased in adult mutants. Finally, the overall SV diameters decreased at *Otof*$^{-/-}$ AZs, while at wt, maturation did not affect the diameters. In conclusion, during maturation, ultrastructural parameters show opposite trends when comparing wt to congenitally deaf *Otof*$^{-/-}$ endbulb AZs. Therefore, the lack of Otof upstream of the CN influences morphological SV pools at individual AZs.

DISCUSSION

In the current study, we tested the hypothesis that functional changes are directly reflected in the presynaptic morphology of the endbulb of Held AZs. Using state-of-the-art ultrastructural methods, we could show that corrupted sound encoding in the cochlea also affects downstream SV numbers and their spatial arrangement at the first central synapse of the auditory pathway. Other key findings of our analysis included increased SV numbers upon maturation in wt and a clear reduction in SV numbers upon a longer period of deafness in *Otof*$^{-/-}$ mice, which was accompanied by smaller SVs in adult mutants.

SV populations at the endbulb of Held AZs

It has been proposed that the SV pool sizes increase during development in the calyx of Held (Iwasaki and Takahashi, 2001; Taschenberger et al., 2002; Taschenberger and von Gersdorff, 2000). Recent serial 3D reconstructions of developing calyces of Held comparing P7 to P21 revealed smaller AZs with a higher SV density in P21 mice (Thomas et al., 2019). In several aspects, the calyx of Held is comparable to the "smaller cousin", the endbulb of Held. Both synapses are part of the auditory pathway and perform ultrafast and temporally precise neurotransmission (Lin et al., 2011). Both comprise large presynaptic terminals that contain hundreds of individual AZs (Nicol and Walmsley, 2002; Ryugo et al., 1996; Sätzler et al., 2002; Wichmann, 2015). In the current study, we found significantly more SVs at adult wt endbulb of Held AZs compared to pre-hearing AZs, which consisted of two distinct SV populations: (i) SVs at a distance of 5–15 nm and (ii) ≥80 nm from the AZ membrane. The 5–15 nm SV population was previously described as a pool of SVs, which are tethered to the AZ membrane via the neuronal soluble N-ethylmaleimide-sensitive factor attachment receptor complex (Cole et al., 2016; Imig et al., 2014; Maus et al., 2020). Studies of hippocampal synapses revealed that this pool was pronounced in docking and priming-deficient mutants, which specifically lack morphologically docked SVs (Imig et al., 2014; Siksou et al., 2009). In Munc13-deficient synapses, SVs accumulated at distances of 8–10 nm from the AZ and for SNAP-25- or Syb-2-deficient synapses from ~4–8 nm (Imig et al., 2014). Moreover, this specific SV pool was interpreted as a supply pool of tethered or loosely docked SVs that likely contribute to synaptic short-term plasticity characteristics of mossy fiber synapses (Maus et al., 2020). Finally, using cryo-ET, SVs connected via multiple ≥5 nm filaments were less abundant at Rab3-interacting molecule (RIM)1-deficient AZs (Fernández-Busnadiego et al., 2013). RIM is known as a critical organizer of SVs in membrane proximity that acts independently of Munc13-1 (Fernández-Busnadiego et al., 2013; Zarebidaki et al., 2020). Therefore, it is conceivable that an accumulation of this specific SV population at 5–15 nm at adult wt endbulb AZs might contribute to an efficient SV recruitment that is required to support reliable neurotransmission with exceedingly high membrane turnover rates.

Docked SVs at wt endbulb AZs during maturation

At wt endbulb of Held AZs, docked SVs numbers and densities remained remarkedly stable throughout maturation. We observed ~3 docked SVs at both, P21 and 6M AZs and ~35–37 docked SVs per μm^2 for all ages. In contrast to previous studies that employed aldehyde-based fixation protocols and a serial reconstruction approach in P25 rats and reported ~15 docked SVs per AZ and 54–83 SVs/μm^2 (Nicol and Walmsley, 2002), we found fewer docked SVs at murine endbulb of Held AZs. This divergence might be explained by either a species difference and/or the different methodologies used: Serial reconstructions have the undisputed advantage that whole AZs can be reconstructed that clearly exceed the volume of our 250 nm tomograms; however, ET enables a higher resolution along the z axis (Harlow et al., 1998).

Consistent with a previous report (Nicol and Walmsley, 2002), we observed highly variable docked SV numbers in all experimental groups. *In vitro* electrophysiological experiments on endbulbs of Held revealed a high variability of functional properties such as the synaptic release probability (P_r) (Oleskevich et al., 2000), which was also observed at the calyx of Held (Fekete et al., 2019). Early on, it was proposed that synaptic P_r may be influenced by the number of docked SVs per AZ (Schikorski and Stevens, 1999; Walmsley et al., 1998), presumably scaling linearly at different synapse types (Branco et al., 2010; Holderith et al., 2012; Murthy et al., 2001). Recent work on hippocampal mossy fiber synapses and Schaffer collateral CA1 synapses revealed a correlation between initial synaptic P_r of the respective synapse type and the number of docked SVs (Maus et al., 2020). At endbulbs of Held AZs, synaptic P_r mainly depends on activity, as shown in a study that investigated short-term depression at endbulbs in different acoustic environments (Zhuang et al., 2020). Thus, it is tempting to speculate that a large range of docked SVs numbers, as found in our study, might contribute to the variability in synapse P_r as found in a previous functional study on endbulbs (Oleskevich et al., 2000).

We want to mention further factors that could influence the variability in SV numbers. The method used in this study might have its limitations. Tomograms from 250-nm sections typically do not include full AZs. To exclude potential errors due to different AZ proportions, we therefore normalized the SV numbers to the AZ area. We approached all our samples in a comparable way and sampled over larger AVCN areas, which ensured that tomograms were taken from different tissue regions. However, properties of the ANFs that project onto BCs might have a greater contribution to variable SV numbers. ANFs can be subdivided functionally and biochemically into three distinct groups that have different sensitivities and spontaneous firing rates (SRs) (Liberman, 1978, 1991; Pfeiffer and Kiang, 1965; Shrestha et al., 2018; Sun et al., 2018). Within the AVCN, SBCs are innervated from all groups, namely low, medium, and high SR ANFs (Liberman 1991), which we cannot distinguish morphologically in our study. Finally, C57BL/6 mice are known to show progressive hearing loss starting at the age of three months (Kujawa and Liberman, 2019; Stamataki et al., 2006). The hearing loss first affects the basal and mid-region of the cochlea and a degeneration of ANFs and ribbon synapses can be detected lastly in the apical region (Stamataki et al., 2006). Hence, age-related changes in the innervation pattern of the CN might be present in our 6M age-group and might contribute to AZ diversity.

Alterations of SV pools at *Otof*$^{-/-}$ endbulb of Held AZs

Spontaneous activity within the auditory system prior to hearing onset shapes the pathway during its development (Sonntag et al., 2009; Tritsch et al., 2010a, 2010b). This non-sensory spontaneous activity seems to be one requirement to build functional AZs (Kerschensteiner, 2014) and is preserved in immature *VGlut3* KO mice, which serve as a model of deafness that lacks IHC-driven activity (Babola et al., 2018). However, type I fibers can be classified molecularly in three subtypes (type Ia, b, c) (Shrestha et al., 2018), and a recent study demonstrated that the subtypes converged at different ratios onto individual target cells (Wang et al., 2021). The molecular differentiation was shown to be disrupted in *VGlut3* KO mice (Shrestha et al., 2018). In our present study, we took advantage of deaf *Otof*$^{-/-}$ mice to investigate the consequences of sensory deprivation on the endbulb of Held individual AZs without directly altering the molecular organization of the endbulb AZs. Otof is essential for IHC ribbon synapse exocytosis and its expression starts from the embryonic stage e16 onwards, with its peak in immunofluorescence at the age of P6 (Roux et al., 2006). At P4, Ca^{2+}–evoked exocytosis in mouse IHC switches from an Otof-independent to an Otof-dependent mechanism (Beurg et al., 2010). Therefore, the complete lack of Otof — and the concomitant abolishment of IHC synaptic sound encoding — throughout maturation may exert structural and functional consequences on the subsequent centers of the auditory pathway. The deletion of Otof dramatically reduces, albeit does not fully abolish the spontaneous miniature excitatory postsynaptic current (mEPSC) frequency, as measured in P9 mice using single bouton recordings at IHC afferent fibers (Takago et al., 2019). Despite this residual activity in these mutants, we could demonstrate a reduction of specific SV populations at individual endbulb *Otof*$^{-/-}$ AZs in adult mice. This matches ultrastructural studies on other deafness models. In 7-month-old shaker-2 mice, next to larger PSDs, fewer SVs were found compared to age-matched hearing controls (Lee et al., 2003). We observed in *Otof*$^{-/-}$ mice significantly fewer docked SVs and a strong reduction of the 5–15 nm SV pool but also SVs at a larger distance to the AZ appeared partially depleted. Additionally, the proportion of docked SVs in membrane proximity was reduced at adult *Otof*$^{-/-}$ AZs. Taken together, at endbulb AZs of Otof-deficient mice, synaptic transmission might be less reliable due to a reduction of several SV populations. Indeed, recordings from BCs in *Otof*$^{-/-}$ mice showed a stronger depression as well as significantly higher synaptic failure rates (Wright et al., 2014).

SV diameters alter at *Otof*$^{-/-}$ endbulb AZs

As a last ultrastructural parameter, we measured the SV diameters, which were previously shown to change upon the lack of activity. Diversity in SV diameters might speak for immaturity or a defective SV formation as shown for a plethora of synapses such as for mammalian ribbon synapses (Strenzke et al., 2016), hippocampal synapses (Imig et al., 2014), and *Drosophila* neuromuscular junctions (Stevens et al., 2012). Moreover, a defective regulation of autophagy can result in larger, more variable SV sizes at synapses (Lüningschrör et al., 2017). A study on monaural conductive hearing loss in rats revealed smaller SVs in earplugged animals, which again increased in size after earplug removal (Clarkson et al., 2016). At endbulbs of Held of normal hearing P20, P44 to P100 mice, SV sizes increased upon development, which was arrested in knockouts for the essential glutamate receptor subunit GluA3 (Antunes et al., 2020). We found that SV diameters in wt remained stable throughout maturation, while in *Otof*$^{-/-}$ endbulbs of Held a decrease in SV sizes was observed. This decrease also applied to docked SVs; therefore, a smaller

quantal size could be assumed at *Otof*$^{-/-}$ endbulbs. However, in *Otof*$^{-/-}$ mice, spontaneous mEPSCs in BCs were found to be significantly larger compared to controls (Wright et al., 2014), which partially contradicts our findings on SV sizes. In contrast, occlusion to abolish auditory input had no significant effect on mEPSC amplitude as recorded at P23 endbulbs (Zhuang et al., 2017) but altered other endbulb properties such as an elevation of P_r (Zhuang et al., 2017, 2020). It should be mentioned that quantal size differences do not always correlate to the SV sizes (Taschenberger et al., 2002) because other mechanisms such as vesicular glutamate concentration can contribute to the measured quantal size (Edwards, 2007; Wu et al., 2007). Future studies are required to tackle these findings using correlative structure-function approaches.

Limitations of the study

In our study, we cannot distinguish which functional properties the analyzed endbulbs of Held initially had (low, medium, high spontaneous rate fibers), which might have contributed to a certain variability of the data. We also did not provide cell physiological experiments along with our morphological findings. Future studies are required to decipher these questions.

Resource availability

Lead contact

Further information and requests for resources and reagents should be directed to and will be fulfilled by the lead contact, Carolin Wichmann (carolin.wichmann@med.uni-goettingen.de).

Materials availability

This study did not generate any new unique reagents.

Data and code availability

Does not apply for this study.

METHODS

All methods can be found in the accompanying Transparent methods supplemental file.

SUPPLEMENTAL INFORMATION

Supplemental information can be found online at https://doi.org/10.1016/j.isci.2021.102282.

ACKNOWLEDGMENTS

We thank A.J. Goldak, C. Senger-Freitag, and S. Gerke for excellent technical support. We also thank O. Diaz for supporting us with IT problems, specifically during the pandemics, and S. Michanski for helping us with Igor. We thank C. Vogl, T. Butola, and T. Alvanos for critical comments on earlier versions of the manuscript. Furthermore, we thank E. Reisinger for the *Otof*$^{-/-}$ mice. This project was funded by the CRC 1286 by the German research Foundation (DFG) to C.W. (TP A4).

AUTHOR CONTRIBUTIONS

C.W. designed and supervised the study. A.H. performed all experiments and analysis, with the help of E.A.S., who significantly contributed in tomogram acquisition and analysis of the P22 and P10 *Otof*$^{-/-}$ mice. M.G. with the help of A.H. performed the statistical analysis of the data. A.H. and C.W. wrote the manuscript with the help of all authors.

DECLARATION OF INTERESTS

The authors declare no competing interests.

Received: October 9, 2020
Revised: January 18, 2021
Accepted: March 3, 2021
Published: April 23, 2021

REFERENCES

Antunes, F.M., Rubio, M.E., and Kandler, K. (2020). Role of GluA3 AMPA receptor subunits in the presynaptic and postsynaptic maturation of synaptic transmission and plasticity of endbulb–bushy cell synapses in the cochlear nucleus. J. Neurosci. *40*, 2471–2484.

Ashida, G., and Carr, C.E. (2011). Sound localization: Jeffress and beyond. Curr. Opin. Neurobiol. *21*, 745–751.

Babalian, A.L., Ryugo, D.K., and Rouiller, E.M. (2003). Discharge properties of identified cochlear nucleus neurons and auditory nerve fibers in response to repetitive electrical stimulation of the auditory nerve. Exp. Brain Res. *153*, 452–460.

Babola, T.A., Li, S., Gribizis, A., Lee, B.J., Issa, J.B., Wang, H.C., Crair, M.C., and Bergles, D.E. (2018). Homeostatic control of spontaneous activity in the developing auditory system. Neuron *99*, 511–524.e5.

Beurg, M., Michalski, N., Safieddine, S., Bouleau, Y., Schneggenburger, R., Chapman, E.R., Petit, C., and Dulon, D. (2010). Control of exocytosis by synaptotagmins and otoferlin in auditory hair cells. J. Neurosci. Official J. Soc. Neurosci. *30*, 13281–13290.

Borst, J.G.G., and Soria van Hoeve, J. (2012). The calyx of held synapse: from model synapse to auditory relay. Annu. Rev. Physiol. *74*, 199–224.

Branco, T., Marra, V., and Staras, K. (2010). Examining size-strength relationships at hippocampal synapses using an ultrastructural measurement of synaptic release probability. J. Struct. Biol. *172*, 203–210.

Brawer, J.R., and Morest, D.K. (1975). Relations between auditory nerve endings and cell types in the cat's anteroventral cochlear nucleus seen with the Golgi method and nomarski optics. J. Comp. Neurol. *160*, 491–506.

Brenowitz, S., and Trussell, L.O. (2001). Maturation of synaptic transmission at end-bulb synapses of the cochlear nucleus. J. Neurosci. *21*, 9487–9498.

Cant, N.B., and Casseday, J.H. (1986). Projections from the anteroventral cochlear nucleus to the lateral and medial superior olivary nuclei. J. Comp. Neurol. *247*, 457–476.

Clarkson, C., Antunes, F.M., and Rubio, M.E. (2016). Conductive hearing loss has long-lasting structural and molecular effects on presynaptic and postsynaptic structures of auditory nerve synapses in the cochlear nucleus. J. Neurosci. *36*, 10214–10227.

Cole, A.A., Chen, X., and Reese, T.S. (2016). A network of three types of filaments organizes synaptic vesicles for storage, mobilization, and docking. J. Neurosci. *36*, 3222–3230.

Colonnier, M. (1968). Synaptic patterns on different cell types in the different laminae of the cat visual cortex. An electron microscope study. Brain Res. *9*, 268–287.

Eddins, A.C., Ozmeral, E.J., and Eddins, D.A. (2018). How aging impacts the encoding of binaural cues and the perception of auditory space. Hearing Res. *369*, 79–89.

Edwards, R.H. (2007). The neurotransmitter cycle and quantal size. Neuron *55*, 835–858.

Fekete, A., Nakamura, Y., Yang, Y.-M., Herlitze, S., Mark, M.D., DiGregorio, D.A., and Wang, L.-Y. (2019). Underpinning heterogeneity in synaptic transmission by presynaptic ensembles of distinct morphological modules. Nat. Commun. *10*, 826.

Fernández-Busnadiego, R., Asano, S., Oprisoreanu, A.-M., Sakata, E., Doengi, M., Kochovski, Z., Zürner, M., Stein, V., Schoch, S., Baumeister, W., and Lučić, V. (2013). Cryo-electron tomography reveals a critical role of RIM1α in synaptic vesicle tethering. J. Cell Biol. *201*, 725–740.

Fernández-Busnadiego, R., Zuber, B., Maurer, U.E., Cyrklaff, M., Baumeister, W., and Lučić, V. (2010). Quantitative analysis of the native presynaptic cytomatrix by cryoelectron tomography. J. Cell Biol. *188*, 145–156.

García-Hernández, S., Abe, M., Sakimura, K., and Rubio, M.E. (2017). Impaired auditory processing and altered structure of the endbulb of Held synapse in mice lacking the GluA3 subunit of AMPA receptors. Hearing Res. *344*, 284–294.

Gómez-Nieto, R., and Rubio, M.E. (2011). Ultrastructure, synaptic organization, and molecular components of bushy cell networks in the anteroventral cochlear nucleus of the rhesus monkey. Neuroscience *179*, 188–207.

Gray, E.G. (1959). Axo-somatic and axo-dendritic synapses of the cerebral cortex. J. Anat. *93*, 420–433.

Grothe, B., Pecka, M., and McAlpine, D. (2010). Mechanisms of sound localization in mammals. Physiol. Rev. *90*, 983–1012.

Gulley, R.L., and Reese, T.S. (1981). Cytoskeletal organization at the postsynaptic complex. J. Cell Biol. *91*, 298–302.

Harlow, M., Ress, D., Koster, A., Marshall, R.M., Schwarz, M., and McMahan, U.J. (1998). Dissection of active zones at the neuromuscular junction by EM tomography. J. Physiology-Paris *92*, 75–78.

Harris, K.M., and Weinberg, R.J. (2012). Ultrastructure of synapses in the mammalian brain. Cold Spring Harbor Perspect. Biol. *4*, a005587.

Harrison, J.M., and Irving, R. (1965). The anterior ventral cochlear nucleus. J. Comp. Neurol. *124*, 15–41.

Harrison, J.M., and Irving, R. (1966). Ascending connections of the anterior ventral cochlear nucleus in the rat. J. Comp. Neurol. *126*, 51–63.

Holderith, N., Lorincz, A., Katona, G., Rózsa, B., Kulik, A., Watanabe, M., and Nusser, Z. (2012). Release probability of hippocampal glutamatergic terminals scales with the size of the active zone. Nat. Neurosci. *15*, 988–997.

Imig, C., Min, S.-W., Krinner, S., Arancillo, M., Rosenmund, C., Südhof, T.C., Rhee, J., Brose, N., and Cooper, B.H. (2014). The morphological and molecular nature of synaptic vesicle priming at presynaptic active zones. Neuron *84*, 416–431.

Iwasaki, S., and Takahashi, T. (2001). Developmental regulation of transmitter release at the calyx of Held in rat auditory brainstem. J. Physiol. *534*, 861–871.

Joris, P.X., Smith, P.H., and Yin, T.C. (1994). Enhancement of neural synchronization in the anteroventral cochlear nucleus. II. Responses in the tuning curve tail. J. Neurophysiol. *71*, 1037–1051.

Joris, Philip X., and Trussell, L.O. (2018). The calyx of held: a hypothesis on the need for reliable timing in an intensity-difference encoder. Neuron *100*, 534–549.

Kaeser, P.S., and Regehr, W.G. (2017). The readily releasable pool of synaptic vesicles. Curr. Opin. Neurobiol. *43*, 63–70.

Keine, C., and Rübsamen, R. (2015). Inhibition shapes acoustic responsiveness in spherical bushy cells. J. Neurosci. *35*, 8579–8592.

Kerschensteiner, D. (2014). Spontaneous network activity and synaptic development. Neuroscientist : A Rev. J. Bringing Neurobiol. Neurol. Psychiatry *20*, 272–290.

Kuenzel, T. (2019). Modulatory influences on time-coding neurons in the ventral cochlear nucleus. Hearing Res. *384*, 107824.

Kujawa, S.G., and Liberman, M.C. (2019). Translating animal models to human therapeutics in noise-induced and age-related hearing loss. Hearing Res. *377*, 44–52.

Landis, D.M., Hall, A.K., Weinstein, L.A., and Reese, T.S. (1988). The organization of cytoplasm at the presynaptic active zone of a central nervous system synapse. Neuron *1*, 201–209.

Lauer, A.M., Connelly, C.J., Graham, H., and Ryugo, D.K. (2013). Morphological characterization of bushy cells and their inputs in the laboratory mouse (Mus musculus) anteroventral cochlear nucleus. PLoS ONE *8*, e73308.

Lee, D.J., Cahill, H.B., and Ryugo, D.K. (2003). Effects of congenital deafness in the cochlear nuclei of Shaker-2 mice: an ultrastructural analysis of synapse morphology in the endbulbs of Held. J. Neurocytology *32*, 229–243.

Liberman, M.C. (1978). Auditory-nerve response from cats raised in a low-noise chamber. The J. Acoust. Soc. America *63*, 442–455.

Liberman, M.C. (1991). Central projections of auditory-nerve fibers of differing spontaneous rate. I. Anteroventral cochlear nucleus. J. Comp. Neurol. *313*, 240–258.

Liberman, M. Charles, and Oliver, M.E. (1984). Morphometry of intracellularly labeled neurons of the auditory nerve: Correlations with functional properties. J. Comp. Neurol. *223*, 163–176.

Limb, C.J., and Ryugo, D.K. (2000). Development of primary axosomatic endings in the

anteroventral cochlear nucleus of mice. J. Assoc. Res. Otolaryngol. *1*, 103–119.

Lin, K.-H., Oleskevich, S., and Taschenberger, H. (2011). Presynaptic Ca2+ influx and vesicle exocytosis at the mouse endbulb of Held: a comparison of two auditory nerve terminals. J. Physiol. *589*, 4301–4320.

R. Lorente de Nó, ed. (1981). The Primary Acoustic Nuclei (Raven Press), pp. 1–177.

Lüningschrör, P., Binotti, B., Dombert, B., Heimann, P., Perez-Lara, A., Slotta, C., Thau-Habermann, N., von Collenberg, C., Karl, F., Damme, M., et al. (2017). Plekhg5-regulated autophagy of synaptic vesicles reveals a pathogenic mechanism in motoneuron disease. Nat. Commun. *8*, 678.

Maus, L., Lee, C., Altas, B., Sertel, S.M., Weyand, K., Rizzoli, S.O., Rhee, J., Brose, N., Imig, C., and Cooper, B.H. (2020). Ultrastructural correlates of presynaptic functional heterogeneity in hippocampal synapses. Cell Rep. *30*, 3632–3643.e8.

Mikaelian, D., and Ruben, R.J. (1965). Development of hearing in the normal Cba-J mouse: correlation of physiological observations with behavioral responses and with cochlear anatomy. Acta Oto-Laryngologica *59*, 451–461.

Moser, T., Neef, A., and Khimich, D. (2006). Mechanisms underlying the temporal precision of sound coding at the inner hair cell ribbon synapse. J. Physiol. *576*, 55–62.

Moser, Tobias, and Starr, A. (2016). Auditory neuropathy — neural and synaptic mechanisms. Nat. Rev. Neurol. *12*, 135–149.

Murthy, V.N., Schikorski, T., Stevens, C.F., and Zhu, Y. (2001). Inactivity produces increases in neurotransmitter release and synapse size. Neuron *32*, 673–682.

Nicol, M.J., and Walmsley, B. (2002). Ultrastructural basis of synaptic transmission between endbulbs of Held and bushy cells in the rat cochlear nucleus. J. Physiol. *539*, 713.

Oleskevich, S., Clements, J., and Walmsley, B. (2000). Release probability modulates short-term plasticity at a rat giant terminal. J. Physiol. *524*, 513–523.

O'Neil, J.N., Connelly, C.J., Limb, C.J., and Ryugo, D.K. (2011). Synaptic morphology and the influence of auditory experience. Hearing Res. *279*, 118–130.

Osen, K.K. (1969). Cytoarchitecture of the cochlear nuclei in the cat. J. Comp. Neurol. *136*, 453–483.

Ostapoff, E.-M., Feng, J.J., and Morest, D.K. (1994). A physiological and structural study of neuron types in the cochlear nucleus. II. Neuron types and their structural correlation with response properties. J. Comp. Neurol. *346*, 19–42.

Pangrsic, T., Lasarow, L., Reuter, K., Takago, H., Schwander, M., Riedel, D., Frank, T., Tarantino, L.M., Bailey, J.S., Strenzke, N., et al. (2010). Hearing requires otoferlin-dependent efficient replenishment of synaptic vesicles in hair cells. Nat. Neurosci. *13*, 869–876.

Paolini, A.G., FitzGerald, J.V., Burkitt, A.N., and Clark, G.M. (2001). Temporal processing from the auditory nerve to the medial nucleus of the trapezoid body in the rat. Hearing Res. *159*, 101–116.

Pfeiffer, R.R., and Kiang, N.Y.-S. (1965). Spike discharge patterns of spontaneous and continuously stimulated activity in the cochlear nucleus of anesthetized cats. Biophysical J. *5*, 301–316.

Pfeiffer, Russell R. (1966). Anteroventral cochlear nucleus:wave forms of extracellularly recorded spike potentials. Science *154*, 667–668.

Redd, E.E., Pongstaporn, T., and Ryugo, D.K. (2000). The effects of congenital deafness on auditory nerve synapses and globular bushy cells in cats. Hearing Res. *147*, 160–174.

Rizzoli, S.O., and Betz, W.J. (2005). Synaptic vesicle pools. Nat. Rev. Neurosci. *6*, 57–69.

Rodríguez-Ballesteros, M., Reynoso, R., Olarte, M., Villamar, M., Morera, C., Santarelli, R., Arslan, E., Medá, C., Curet, C., Völter, C., et al. (2008). A multicenter study on the prevalence and spectrum of mutations in the otoferlin gene (OTOF) in subjects with nonsyndromic hearing impairment and auditory neuropathy. Hum. Mutat. *29*, 823–831.

Rouiller, E.M., Cronin-Schreiber, R., Fekete, D.M., and Ryugo, D.K. (1986). The central prod ections of intracellularly labeled auditory nerve fibers in cats: an analysis of terminal morphology. J. Comp. Neurol. *249*, 261–278.

Roux, I., Safieddine, S., Nouvian, R., Grati, M., Simmler, M.-C., Bahloul, A., Perfettini, I., Le Gall, M., Rostaing, P., Hamard, G., et al. (2006). Otoferlin, defective in a human deafness form, is essential for exocytosis at the auditory ribbon synapse. Cell *127*, 277–289.

Ryugo, D.K., and Fekete, D.M. (1982). Morphology of primary axosomatic endings in the anteroventral cochlear nucleus of the cat: a study of the endbulbs of Held. J. Comp. Neurol. *210*, 239–257.

Ryugo, D.K., Pongstaporn, T., Huchton, D.M., and Niparko, J.K. (1997). Ultrastructural analysis of primary endings in deaf white cats: Morphologic alterations in endbulbs of held. J. Comp. Neurol. *385*, 230–244.

Ryugo, D., and Spirou, G. (2009). Auditory system: giant synaptic terminals, endbulbs and calyces. In New Encyclopedia of Neuroscience (Academic Press), pp. 759–770.

Ryugo, David K., Wu, M.M., and Pongstaporn, T. (1996). Activity-related features of synapse morphology: a study of endbulbs of Held. J. Comp. Neurol. *365*, 141–158.

Safieddine, S., and Wenthold, R.J. (1999). SNARE complex at the ribbon synapses of cochlear hair cells: analysis of synaptic vesicle- and synaptic membrane-associated proteins. Eur. J. Neurosci. *11*, 803–812.

Sätzler, K., Söhl, L.F., Bollmann, J.H., Borst, J.G.G., Frotscher, M., Sakmann, B., and Lübke, J.H.R. (2002). Three-dimensional reconstruction of a calyx of held and its postsynaptic principal neuron in the medial nucleus of the trapezoid body. J. Neurosci. *22*, 10567–10579.

Schikorski, T., and Stevens, C.F. (1999). Quantitative fine-structural analysis of olfactory cortical synapses. Proc. Natl. Acad. Sci. United States America *96*, 4107–4112.

Schikorski, Thomas, and Stevens, C.F. (2001). Morphological correlates of functionally defined synaptic vesicle populations. Nat. Neurosci. *4*, 391–395.

Shrestha, B.R., Chia, C., Wu, L., Kujawa, S.G., Liberman, M.C., and Goodrich, L.V. (2018). Sensory neuron diversity in the inner ear is shaped by activity. Cell *174*, 1229–1246.e17.

Siksou, L., Rostaing, P., Lechaire, J.-P., Boudier, T., Ohtsuka, T., Fejtová, A., Kao, H.-T., Greengard, P., Gundelfinger, E.D., Triller, A., and Marty, S. (2007). Three-dimensional architecture of presynaptic terminal cytomatrix. J. Neurosci. *27*, 6868–6877.

Siksou, L., Varoqueaux, F., Pascual, O., Triller, A., Brose, N., and Marty, S. (2009). A common molecular basis for membrane docking and functional priming of synaptic vesicles. Eur. J. Neurosci. *30*, 49–56.

Smith, P.H., Joris, P.X., and Yin, T.C.T. (1993). Projections of physiologically characterized spherical bushy cell axons from the cochlear nucleus of the cat: Evidence for delay lines to the medial superior olive. J. Comp. Neurol. *331*, 245–260.

Sonntag, M., Englitz, B., Kopp-Scheinpflug, C., and Rübsamen, R. (2009). Early postnatal development of spontaneous and acoustically evoked discharge activity of principal cells of the medial nucleus of the trapezoid body: an in vivo study in mice. J. Neurosci. *29*, 9510.

Spirou, G.A., Rager, J., and Manis, P.B. (2005). Convergence of auditory-nerve fiber projections onto globular bushy cells. Neuroscience *136*, 843–863.

Stamataki, S., Francis, H.W., Lehar, M., May, B.J., and Ryugo, D.K. (2006). Synaptic alterations at inner hair cells precede spiral ganglion cell loss in aging C57BL/6J mice. Hearing Res. *221*, 104–118.

Stevens, R.J., Akbergenova, Y., Jorquera, R.A., and Littleton, J.T. (2012). Abnormal synaptic vesicle biogenesis in Drosophila synaptogyrin mutants. J. Neurosci. *32*, 18054–18067.

Strenzke, N., Chakrabarti, R., Al-Moyed, H., Müller, A., Hoch, G., Pangrsic, T., Yamanbaeva, G., Lenz, C., Pan, K.-T., Auge, E., et al. (2016). Hair cell synaptic dysfunction, auditory fatigue and thermal sensitivity in otoferlin Ile515Thr mutants. EMBO J. *35*, 2519–2535.

Sun, S., Babola, T., Pregernig, G., So, K.S., Nguyen, M., Su, S.-S.M., Palermo, A.T., Bergles, D.E., Burns, J.C., and Müller, U. (2018). Hair cell mechanotransduction regulates spontaneous activity and spiral ganglion subtype specification in the auditory system. Cell *174*, 1247–1263.e15.

Takago, H., Oshima-Takago, T., and Moser, T. (2019). Disruption of otoferlin alters the mode of exocytosis at the mouse inner hair cell ribbon synapse. Front. Mol. Neurosci. *11*, 492.

Tao, C.-L., Liu, Y.-T., Sun, R., Zhang, B., Qi, L., Shivakoti, S., Tian, C.-L., Zhang, P., Lau, P.-M., Zhou, Z.H., and Bi, G.-Q. (2018). Differentiation and characterization of excitatory and inhibitory synapses by cryo-electron tomography and correlative microscopy. J. Neurosci. *38*, 1493–1510.

Taschenberger, H., Leão, R.M., Rowland, K.C., Spirou, G.A., and von Gersdorff, H. (2002). Optimizing synaptic architecture and efficiency for high-frequency transmission. Neuron *36*, 1127–1143.

Taschenberger, H., and von Gersdorff, H. (2000). Fine-tuning an auditory synapse for speed and fidelity: developmental changes in presynaptic waveform, EPSC kinetics, and synaptic plasticity. J. Neurosci. *20*, 9162–9173.

Tatsuoka, H., and Reese, T.S. (1989). New structural features of synapses in the anteroventral cochlear nucleus prepared by direct freezing and freeze-substitution. J. Comp. Neurol. *290*, 343–357.

Thomas, C.I., Keine, C., Okayama, S., Satterfield, R., Musgrove, M., Guerrero-Given, D., Kamasawa, N., and Young, S.M. (2019). Presynaptic mitochondria volume and abundance increase during development of a high-fidelity synapse. J. Neurosci. *39*, 7994–8012.

Tolbert, L.P., and Morest, D.K. (1982). The neuronal architecture of the anteroventral cochlear nucleus of the cat in the region of the cochlear nerve root: Golgi and Nissl methods. Neuroscience *7*, 3013–3030.

Tritsch, N.X., Rodríguez-Contreras, A., Crins, T.T.H., Wang, H.C., Borst, J.G.G., and Bergles, D.E. (2010a). Calcium action potentials in hair cells pattern auditory neuron activity before hearing onset. Nat. Neurosci. *13*, 1050–1052.

Tritsch, N.X., Zhang, Y.-X., Ellis-Davies, G., and Bergles, D.E. (2010b). ATP-induced morphological changes in supporting cells of the developing cochlea. Purinergic Signal. *6*, 155–166.

Varga, R., Avenarius, M.R., Kelley, P.M., Keats, B.J., Berlin, C.I., Hood, L.J., Morlet, T.G., Brashears, S.M., Starr, A., Cohn, E.S., et al. (2006). OTOF mutations revealed by genetic analysis of hearing loss families including a potential temperature sensitive auditory neuropathy allele. J. Med. Genet. *43*, 576–581.

Walmsley, B., Alvarez, F.J., and Fyffe, R.E.W. (1998). Diversity of structure and function at mammalian central synapses. Trends Neurosciences *21*, 81–88.

Wang, Y., and Manis, P.B. (2006). Temporal coding by cochlear nucleus bushy cells in DBA/2J mice with early onset hearing loss. J. Assoc. Res. Otolaryngol. *7*, 412–424.

Wang, Y., O'Donohue, H., and Manis, P. (2011). Short-term plasticity and auditory processing in the ventral cochlear nucleus of normal and hearing-impaired animals. Hearing Res. *279*, 131–139.

Wang, M., Zhang, C., Lin, S., Wang, Y., Seicol, B.J., Ariss, R.W., and Xie, R. (2021). Biased auditory nerve central synaptopathy is associated with age-related hearing loss. J. Physiol. *599*, 1833–1854, https://doi.org/10.1113/JP281014.

Warr, W.B. (1966). Fiber degeneration following lesions in the anterior ventral cochlear nucleus of the cat. Exp. Neurol. *14*, 453–474.

Watanabe, S., Rost, B.R., Camacho-Pérez, M., Davis, M.W., Söhl-Kielczynski, B., Rosenmund, C., and Jorgensen, E.M. (2013). Ultrafast endocytosis at mouse hippocampal synapses. Nature *504*, 242–247.

Wesseling, J.F., Phan, S., Bushong, E.A., Siksou, L., Marty, S., Pérez-Otaño, I., and Ellisman, M. (2019). Sparse force-bearing bridges between neighboring synaptic vesicles. Brain Struct. Funct. *224*, 3263–3276.

Wichmann, C. (2015). Molecularly and structurally distinct synapses mediate reliable encoding and processing of auditory information. Hearing Res. *330*, 178–190.

Willard, F.H., and Ryugo, D.K. (1983). Anatomy of the central auditory system. In The Auditory Psychobiology of the Mouse, J.F. Willott, ed. (Charles C Thomas), pp. 201–304.

Wright, S., Hwang, Y., and Oertel, D. (2014). Synaptic transmission between end bulbs of Held and bushy cells in the cochlear nucleus of mice with a mutation in Otoferlin. J. Neurophysiol. *112*, 3173–3188.

Wu, L.-G., Ryan, T.A., and Lagnado, L. (2007). Modes of vesicle retrieval at ribbon synapses, calyx-type synapses, and small central synapses. J. Neurosci. *27*, 11793–11802.

Wu, S.H., and Oertel, D. (1984). Intracellular injection with horseradish peroxidase of physiologically characterized stellate and bushy cells in slices of mouse anteroventral cochlear nucleus. J. Neurosci. Official J. Soc. Neurosci. *4*, 1577–1588.

Yang, H., and Xu-Friedman, M.A. (2010). Developmental mechanisms for suppressing the effects of delayed release at the endbulb of held. J. Neurosci. *30*, 11466–11475.

Yasunaga, S., Grati, M., Cohen-Salmon, M., El-Amraoui, A., Mustapha, M., Salem, N., El-Zir, E., Loiselet, J., and Petit, C. (1999). A mutation in OTOF, encoding otoferlin, a FER-1-like protein, causes DFNB9, a nonsyndromic form of deafness. Nat. Genet. *21*, 363–369.

Zarebidaki, F., Camacho, M., Brockmann, M.M., Trimbuch, T., Herman, M.A., and Rosenmund, C. (2020). Disentangling the roles of RIM and Munc13 in synaptic vesicle localization and neurotransmission. J. Neurosci. *40*, 9372–9385.

Zhuang, X., Sun, W., and Xu-Friedman, M.A. (2017). Changes in properties of auditory nerve synapses following conductive hearing loss. J. Neurosci. *37*, 323–332.

Zhuang, X., Wong, N.F., Sun, W., and Xu-Friedman, M.A. (2020). Mechanisms and functional consequences of presynaptic homeostatic plasticity at auditory nerve synapses. J. Neurosci. *40*, 6896–6909.

iScience, Volume *24*

Supplemental information

Ultrastructural maturation of the endbulb of Held active zones comparing wild-type and otoferlin-deficient mice

Anika Hintze, Mehmet Gültas, Esther A. Semmelhack, and Carolin Wichmann

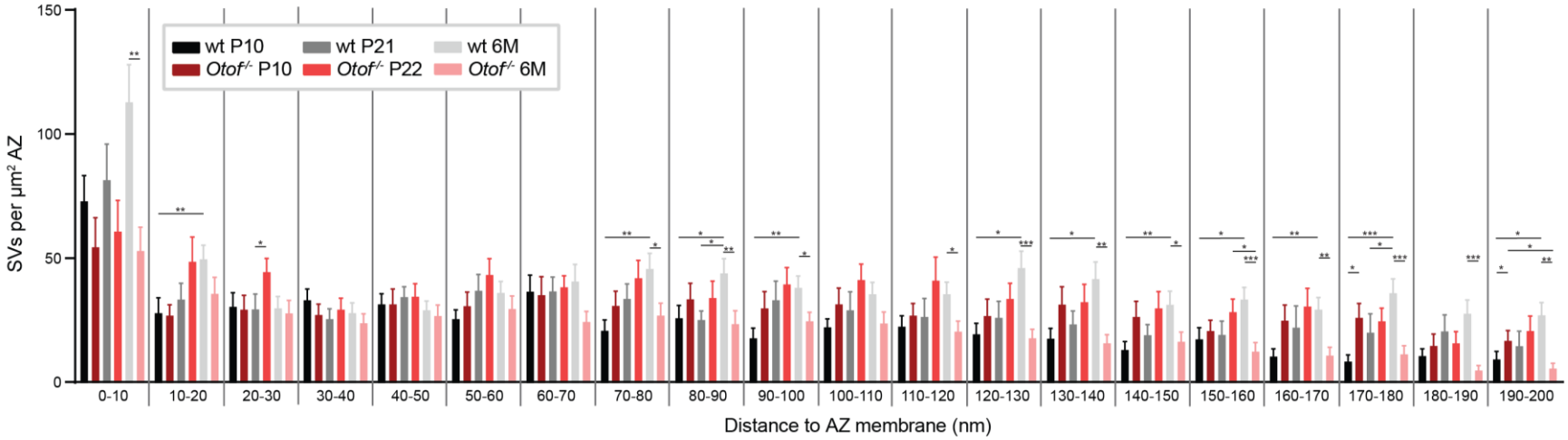

Figure S1. SV distribution at wt and *Otof*$^{-/-}$ endbulb AZs, Related to Figure 2. Number of SVs within 10 nm bins normalized to the AZ area. Data are presented as bar graph that represent mean ± SEM. *p < 0.05; **p < 0.01; ***p < 0.001. wt P10 (N = 4; n = 24), *Otof*$^{-/-}$ P10 (N = 3; n = 22), wt P21 (N = 3; n = 22), *Otof*$^{-/-}$ P22 (N = 3; n = 23), wt 6M (N = 3; n = 29) and *Otof*$^{-/-}$ 6M (N = 3; n = 23), (N, number of animals; n, number of AZs). All values see Tables S6-S10.

Parameter		wt P10	wt P21	wt 6M	*p*-value
AZ area (µm²)		0.1040 ± 0.0089 (0.0892)	0.1045 ± 0.0090 (0.1036)	0.0816 ± 0.0042 (0.0813)	ANOVA: $p = 0.0384$, Tukey´s: wt P10 vs. wt P21: $p = 0.9991$ wt P10 vs. wt 6M: $p = 0.0739$ wt P21 vs. wt 6M: $p = 0.0759$
SVs per AZ	all SVs	45.88 ± 4.25 (43.00)	54.09 ± 5.94 (48.50)	63.52 ± 5.63 (55.00)	$p = 0.0643$
	docked SVs	3.54 ± 0.70 (2.50)	3.05 ± 0.63 (2.50)	2.97 ± 0.51 (3.00)	$p = 0.8403$
	membrane-proximal SVs	12.17 ± 1.32 (12.00)	12.86 ± 1.51 (11.00)	14.48 ± 1.18 (13.00)	$p = 0.4544$
SVs per µm² AZ	all SVs	477.4 ± 44.1 (445.6)	594.2 ± 89.7 (480.4)	801.5 ± 65.67 (765.5)	wt P10 vs. wt P21: $p = 0.4771$ wt P10 vs. wt 6M: $^{**}p = 0.0026$ wt P21 vs. wt 6M: $p = 0.0850$
	docked SVs	36.83 ± 6.64 (26.88)	35.19 ± 8.93 (21.24)	37.00 ± 7.15 (30.30)	$p = 0.8077$
	membrane-proximal SVs	128.5 ± 16.56 (112.8)	135.6 ± 16.2 (111.7)	184.1 ± 13.4 (189.6)	wt P10 vs. wt P21: $p = 0.9472$ wt P10 vs. wt 6M: $^{*}p = 0.0266$ wt P21 vs. wt 6M: $p = 0.0688$
	0-5 nm	60.22 ± 9.19 (42.35)	51.89 ± 10.37 (37.00)	71.81 ± 11.68 (49.23)	$p = 0.4217$
	5-10 nm	13.00 ± 3.04 (9.17)	29.83 ± 6.18 (21.09)	41.31 ± 5.71 (39.50)	wt P10 vs. wt P21: $^{*}p = 0.0236$ wt P10 vs. wt 6M: $^{***}p = 0.0002$ wt P21 vs. wt 6M: $p = 0.8236$
	10-15 nm	18.01 ± 4.17 (13.03)	17.70 ± 3.23 (16.37)	31.66 ± 3.85 (28.60)	wt P10 vs. wt P21: $p > 0.9999$ wt P10 vs. wt 6M: $^{*}p = 0.0171$ wt P21 vs. wt 6M: $p = 0.0500$
	15-20 nm	10.14 ± 2.49 (7.34)	15.94 ± 4.01 (8.47)	18.13 ± 2.55 (18.42)	$p = 0.1011$
	20-25 nm	15.57 ± 3.70 (12.98)	16.84 ± 3.67 (14.41)	11.79 ± 2.10 (12.31)	$p = 0.6322$
	25-30 nm	15.10 ± 3.61 (8.11)	12.88 ± 3.20 (7.65)	18.29 ± 3.29 (11.83)	$p = 0.4572$
	30-35 nm	13.64 ± 2.52 (13.24)	13.04 ± 2.55 (12.87)	15.05 ± 2.57 (16.15)	$p = 0.8446$
	35-40 nm	19.69 ± 3.00 (17.15)	12.66 ± 2.94 (9.16)	13.1 ± 2.68 (10.56)	KW: $p = 0.0414$, Dunn's: wt P10 vs. wt P21: $p = 0.0994$ wt P10 vs. wt 6M: $p = 0.0715$ wt P21 vs. wt 6M: $p > 0.9999$
	40-80 nm	115.1 ± 11.2 (99.4)	142.5 ± 17.2 (135.2)	152.3 ± 13.4 (145.3)	$p = 0.1495$
	80-120 nm	89.10 ± 10.28 (82.06)	114.6 ± 20.4 (82.79)	154.0 ± 12.56 (165.8)	wt P10 vs. wt P21: $p = 0.4634$ wt P10 vs. wt 6M: $^{**}p = 0.0051$ wt P21 vs. wt 6M: $p = 0.1402$
	120-160 nm	68.29 ± 11.34 (68.50)	88.30 ± 16.71 (69.24)	153.2 ± 18.75 (130.4)	wt P10 vs. wt P21: $p = 0.6883$ wt P10 vs. wt 6M: $^{**}p = 0.0010$

					wt P21 vs. wt 6M: *p = 0.0181
	160-200 nm	39.61 ± 8.66 (27.61)	78.09 ± 25.73 (35.87)	120.9 ± 16.6 (98.5)	wt P10 vs. wt P21: p = 0.8539 wt P10 vs. wt 6M: **p = 0.0010 wt P21 vs. wt 6M: p = 0.0526
Diameter (nm)	all SVs	51.46 ± 0.50 (51.65)	50.03 ± 0.74 (50.28)	50.62 ± 0.66 (50.37)	p = 0.3235
	docked SVs	50.32 ± 0.72 (50.37)	48.15 ± 1.08 (48.04)	50.29 ± 0.76 (50.28)	p = 0.1558
	membrane-proximal SVs	51.58 ± 0.63 (51.57)	49.73 ± 0.72 (49.99)	50.72 ± 0.76 (50.22)	p = 0.2212
Ratio	0-2/0-40 nm	0.2265 ± 0.0355 (0.1548)	0.1925 ± 0.0393 (0.1583	0.1579 ± 0.0239 (0.1250)	p = 0.3096

Table S1. Quantitative analysis of SV numbers, diameters and the AZ area of wt AZs, Related to Figure 2-6.

Parameter		***Otof*$^{-/-}$ P10**	***Otof*$^{-/-}$ P22**	***Otof*$^{-/-}$ 6M**	***p*-value**
AZ area (µm^2)		0.0944 ± 0.0077 (0.0890)	0.0919 ± 0.0079 (0.0831)	0.0932 ± 0.0057 (0.0933)	p = 0.9415
SVs per AZ	all SVs	49.00 ± 6.38 (39.00)	66.64 ± 8.73 (66.00)	39.61 ± 4.68 (37.00)	*Otof*$^{-/-}$ P10 vs. *Otof*$^{-/-}$ P22: p = 0.1667 *Otof*$^{-/-}$ P10 vs. *Otof*$^{-/-}$ 6M: p = 0.5874 *Otof*$^{-/-}$ P22 vs. *Otof*$^{-/-}$ 6M: *p = 0.0163
	docked SVs	2.73 ± 0.46 (3.00)	2.44 ± 0.84 (1.00)	1.83 ± 0.56 (1.00)	p = 0.0891
	membrane-proximal SVs	8.86 ± 1.13 (7.50)	15.39 ± 2.11 (12.00)	10.78 ± 1.09 (12.00)	*Otof*$^{-/-}$ P10 vs. *Otof*$^{-/-}$ P22: *p = 0.0104 *Otof*$^{-/-}$ P10 vs. *Otof*$^{-/-}$ 6M: p = 0.6526 *Otof*$^{-/-}$ P22 vs. *Otof*$^{-/-}$ 6M: p = 0.0886
SVs per µm^2 AZ	all SVs	579.5 ± 81.6 (453.6)	726.0 ± 76.14 (725.2)	431.3 ± 46.38 (438.2)	*Otof*$^{-/-}$ P10 vs. *Otof*$^{-/-}$ P22: p = 0.3042 *Otof*$^{-/-}$ P10 vs. *Otof*$^{-/-}$ 6M: p = 0.2959 *Otof*$^{-/-}$ P22 vs. *Otof*$^{-/-}$ 6M: **p = 0.0099
	docked SVs	34.89 ± 6.40 (35.94)	24.66 ± 7.39 (13.25)	22.06 ± 6.95 (12.51)	p = 0.1140
	membrane-proximal SVs	103.8 ± 14.6 (90.8)	162.9 ± 14.6 (145.5)	117.5 ± 10.8 (105.1)	*Otof*$^{-/-}$ P10 vs. *Otof*$^{-/-}$ P22: **p = 0.0081 *Otof*$^{-/-}$ P10 vs. *Otof*$^{-/-}$ 6M: p = 0.7555 *Otof*$^{-/-}$ P22 vs. *Otof*$^{-/-}$ 6M: *p = 0.0490
	0-5 nm	42.58 ± 7.85 (36.33)	33.87 ± 9.19 (23.80)	32.30 ± 7.15 (21.43)	p = 0.4598
	5-10 nm	12.05 ± 5.32 (0.00)	30.68 ± 4.45 (34.05)	20.83 ± 4.82 (13.33)	*Otof*$^{-/-}$ P10 vs. *Otof*$^{-/-}$ P22: **p = 0.0011 *Otof*$^{-/-}$ P10 vs. *Otof*$^{-/-}$ 6M: p = 0.2319 *Otof*$^{-/-}$ P22 vs. *Otof*$^{-/-}$ 6M: p = 0.2109
	10-15 nm	12.12 ± 3.09 (10.05)	29.81 ± 7.31 (16.16)	18.02 ± 3.52 (14.96)	p = 0.2624
	15-20 nm	14.98 ± 2.93 (12.24)	19.05 ± 3.93 (13.34)	17.91 ± 4.28 (12.91)	p = 0.7388

	20-25 nm	14.17 ± 2.96 (10.12)	20.79 ± 3.85 (19.82)	14.28 ± 2.73 (16.15)	$p = 0.2555$
	25-30 nm	15.42 ± 3.114 (11.98)	23.84 ± 3.83 (26.69)	13.74 ± 3.28 (10.44)	$p = 0.1012$
	30-35 nm	16.19 ± 3.80 (13.69)	13.37 ± 2.23 (12.57)	11.54 ± 2.23 (10.09)	$p = 0.5094$
	35-40 nm	11.23 ± 2.42 (10.62)	16.13 ± 2.95 (14.95)	12.53 ± 2.45 (12.57)	$p = 0.3971$
	40-80 nm	129.1 ± 16.1 (120.5)	158.9 ± 16.3 (138.9)	108.4 ± 12.08 (85.71)	$p = 0.0601$
	80-120 nm	122.5 ± 18.3 (93.1)	156.6 ± 22.7 (171.7)	92.95 ± 13.17 (77.47)	$p = 0.0560$
	120-160 nm	106.1 ± 19.4 (66.7)	124.9 ± 18.58 (109.0)	63.03 ± 8.99 (62.64)	*Otof*$^{-/-}$ P10 vs. *Otof*$^{-/-}$ P22: $p = 0.6934$ *Otof*$^{-/-}$ P10 vs. *Otof*$^{-/-}$ 6M: $p = 0.1575$ *Otof*$^{-/-}$ P22 vs. *Otof*$^{-/-}$ 6M: $*p = 0.0230$
	160-200 nm	83.14 ± 17.60 (52.28)	92.32 ± 16.93 (62.86)	33.19 ± 8.12 (16.15)	*Otof*$^{-/-}$ P10 vs. *Otof*$^{-/-}$ P22: $p > 0.9999$ *Otof*$^{-/-}$ P10 vs. *Otof*$^{-/-}$ 6M: $p = 0.0503$ *Otof*$^{-/-}$ P22 vs. *Otof*$^{-/-}$ 6M: $*p = 0.0151$
Diameter (nm)	all SVs	54.87 ± 0.90 (55.15)	52.23 ± 1.11 (52.28)	50.63 ± 1.03 (49.94)	*Otof*$^{-/-}$ P10 vs. *Otof*$^{-/-}$ P22: $p = 0.1698$ *Otof*$^{-/-}$ P10 vs. *Otof*$^{-/-}$ 6M: $*p = 0.0128$ *Otof*$^{-/-}$ P22 vs. *Otof*$^{-/-}$ 6M: $p = 0.5060$
	docked SVs	54.99 ± 1.52 (56.10)	51.00 ± 1.83 (49.70)	46.23 ± 1.03 (47.70)	*Otof*$^{-/-}$ P10 vs. *Otof*$^{-/-}$ P22: $p = 0.1517$ *Otof*$^{-/-}$ P10 vs. *Otof*$^{-/-}$ 6M: $***p = 0.0003$ *Otof*$^{-/-}$ P22 vs. *Otof*$^{-/-}$ 6M: $p = 0.0811$
	membrane-proximal SVs	55.36 ± 1.14 (55.35)	51.28 ± 0.98 (51.65)	50.87 ± 1.09 (49.91)	*Otof*$^{-/-}$ P10 vs. *Otof*$^{-/-}$ P22: $*p = 0.0247$ *Otof*$^{-/-}$ P10 vs. *Otof*$^{-/-}$ 6M: $*p = 0.0119$ *Otof*$^{-/-}$ P22 vs. *Otof*$^{-/-}$ 6M: $p = 0.9588$
Ratio	0-2/0-40 nm	0.2326 ± 0.0334 (0.2679)	0.1102 ± 0.0276 (0.0741)	0.1203 ± 0.0304 (0.0769)	*Otof*$^{-/-}$ P10 vs. *Otof*$^{-/-}$ P22: $*p = 0.0168$ *Otof*$^{-/-}$ P10 vs. *Otof*$^{-/-}$ 6M: $*p = 0.0308$ *Otof*$^{-/-}$ P22 vs. *Otof*$^{-/-}$ 6M: $p = 0.9699$

Table S2. Quantitative analysis of SV numbers, diameters and the AZ area of *Otof*$^{-/-}$ AZs, Related to Figure 2-6.

Parameter		wt P10	*Otof*$^{-/-}$ P10	*p*-value
AZ area (µm²)		0.1040 ± 0.0089 (0.0892)	0.0944 ± 0.0077 (0.0890)	*p* = 0.8107
SVs per AZ	all SVs	45.88 ± 4.25 (43.00)	49.00 ± 6.38 (39.00)	*p* = 0.6860
	docked SVs	3.54 ± 0.70 (2.50)	2.73 ± 0.46 (3.00)	*p* = 0.7224
	membrane-proximal SVs	12.17 ± 1.32 (12.00)	8.86 ± 1.13 (7.50)	*p* = 0.0631
SVs per µm² AZ	all SVs	477.4 ± 44.1 (445.6)	579.5 ± 81.6 (453.6)	*p* = 0.6860
	docked SVs	36.83 ± 6.64 (26.88)	34.89 ± 6.40 (35.94)	*p* = 0.8961
	membrane-proximal SVs	128.5 ± 16.56 (112.8)	103.8 ± 14.6 (90.8)	*p* = 0.2943
	0-5 nm	60.22 ± 9.19 (42.35)	42.58 ± 7.85 (36.33)	*p* = 0.1514
	5-10 nm	13.00 ± 3.04 (9.17	12.05 ± 5.32 (0.00)	*p* = 0.2744
	10-15 nm	18.01 ± 4.17 (13.03)	12.12 ± 3.09 (10.05)	*p* = 0.4650
	15-20 nm	10.14 ± 2.49 (7.34)	14.98 ± 2.93 (12.24)	*p* = 0.2123
	20-25 nm	15.57 ± 3.70 (12.98)	14.17 ± 2.96 (10.12)	*p* = 0.9479
	25-30 nm	15.10 ± 3.61 (8.11)	15.42 ± 3.11 (11.98)	*p* = 0.6950
	30-35 nm	13.64 ± 2.52 (13.24)	16.19 ± 3.80 (13.69)	*p* = 0.7357
	35-40 nm	19.69 ± 3.00 (17.15)	11.23 ± 2.42 (10.62)	**p* = 0.0187
	40-80 nm	115.1 ± 11.2 (99.4)	129.1 ± 16.1 (120.5)	*p* = 0.4794
	80-120 nm	89.10 ± 10.28 (82.06)	122.5 ± 18.3 (93.1)	*p* = 0.1210
	120-160 nm	68.29 ± 11.34 (68.50)	106.1 ± 19.4 (66.7)	*p* = 0.5737
	160-200 nm	39.61 ± 8.66 (27.61)	83.14 ± 17.60 (52.28)	**p* = 0.0497
Diameter (nm)	all SVs	51.46 ± 0.50 (51.65)	54.87 ± 0.90 (55.15)	***p* = 0.0022
	docked SVs	50.32 ± 0.72 (50.37)	54.99 ± 1.52 (56.10)	**p* = 0.0104
	membrane-proximal SVs	51.58 ± 0.63 (51.57)	55.36 ± 1.14 (55.35)	***p* = 0.0066
Ratio	0-2/0-40 nm	0.2265 ± 0.0355 (0.1548)	0.2326 ± 0.0334 (0.2679)	*p* = 0.9011

Table S3. Quantitative analysis of SV numbers, diameters and the AZ area of P10 wt and *Otof*$^{-/-}$ mice, Related to Figure 2-6.

Parameter		wt P21	*Otof*$^{-/-}$ P22	*p*-value
AZ area (µm²)		0.1045 ± 0.0090 (0.1036)	0.0919 0.0079 (0.0831)	*p* = 0.2496
SVs per AZ	all SVs	54.09 ± 5.94 (48.50)	66.64 ± 8.73 (66.00)	*p* = 0.2423
	docked SVs	3.05 ± 0.63 (2.50)	2.44 ± 0.84 (1.00)	*p* = 0.2216
	membrane-proximal SVs	12.86 ± 1.51 (11.00)	15.39 ± 2.11 (12.00)	*p* = 0.5578
SVs per µm² AZ	all SVs	594.2 ± 89.7 (480.4)	726.0 ± 76.14 (725.2)	*p* = 0.1474
	docked SVs	35.19 ± 8.93 (21.24)	24.66 ± 7.39 (13.25)	*p* = 0.2591
	membrane-proximal SVs	135.6 ± 16.2 (111.7)	162.9 ± 14.6 (145.5)	*p* = 0.1234
	0-5 nm	51.89 ± 10.37 (37.00	33.87 ± 9.19 (23.80)	*p* = 0.0655
	5-10 nm	29.83 ± 6.18 (21.09)	30.68 ± 4.45 (34.05)	*p* = 0.4109
	10-15 nm	17.70 ± 3.23 (16.37)	29.81 ± 7.31 (16.16)	*p* = 0.6692
	15-20 nm	15.94 ± 4.01 (8.47)	19.05 ± 3.93 (13.34)	*p* = 0.5286
	20-25 nm	16.84 ± 3.67 (14.41)	20.79 ± 3.85 (19.82)	*p* = 0.3919
	25-30 nm	12.88 ± 3.20 (7.65)	23.84 ± 3.83 (26.69)	**p* = 0.0379
	30-35 nm	13.04 ± 2.55 (12.87)	13.37 ± 2.23 (12.57)	*p* = 0.8573

	35-40 nm	12.66 ± 2.94 (9.16)	16.13 ± 2.95 (14.95)	$p = 0.3211$
	40-80 nm	142.5 ± 17.2 (135.2)	158.9 ± 16.3 (138.9)	$p = 0.4174$
	80-120 nm	114.6 ± 20.4 (82.79)	156.6 ± 22.7 (171.7)	$p = 0.1350$
	120-160 nm	88.30 ± 16.71 (69.24)	124.9 ± 18.58 (109.0)	$p = 0.0931$
	160-200 nm	78.09 ± 25.73 (35.87)	92.32 ± 16.93 (62.86)	$p = 0.1976$
Diameter (nm)	all SVs	50.03 ± 0.74 (50.28)	52.23 ± 1.11 (52.28)	$p = 0.1079$
	docked SVs	48.15 ± 1.08 (48.04)	51.00 ± 1.83 (49.70)	$p = 0.1937$
	membrane-proximal SVs	49.73 ± 0.72 (49.99)	51.28 ± 0.98 (51.65)	$p = 0.2073$
Ratio	0-2/0-40 nm	0.1925 ± 0.0393 (0.1583)	0.1102 ± 0.0276 (0.0741)	$p = 0.1646$

Table S4. Quantitative analysis of SV numbers, diameters and the AZ area of P21/22 wt and *Otof*$^{-/-}$ mice, Related to Figure 2-6.

Parameter		**wt 6M**	***Otof*$^{-/-}$ 6M**	***p*-value**
AZ area (µm^2)		0.0816 ± 0.0042 (0.0813)	0.0932 0.0057 (0.0933)	$p = 0.1980$
SVs per AZ	all SVs	63.52 ± 5.63 (55.00)	39.61 ± 4.68 (37.00)	$^{**}p = 0.0020$
	docked SVs	2.97 ± 0.51 (3.00)	1.83 ± 0.56 (1.00)	$^{*}p = 0.0379$
	membrane-proximal SVs	14.48 ± 1.18 (13.00)	10.78 ± 1.09 (12.00)	$p = 0.0695$
SVs per µm^2 AZ	all SVs	801.5 ± 65.67 (765.5)	431.3 ± 46.38 (438.2)	$^{****}p < 0.0001$
	docked SVs	37.00 ± 7.15 (30.30)	22.06 ± 6.95 (12.51)	$^{*}p = 0.0317$
	membrane-proximal SVs	184.1 ± 13.4 (189.6)	117.5 ± 10.8 (105.1)	$^{***}p = 0.0003$
	0-5 nm	71.81 ± 11.68 (49.23)	32.30 ± 7.15 (21.43)	$^{**}p = 0.0036$
	5-10 nm	41.31 ± 5.71 (39.50)	20.83 ± 4.82 (13.33)	$^{*}p = 0.0110$
	10-15 nm	31.66 ± 3.85 (28.60)	18.02 ± 3.52 (14.96)	$^{*}p = 0.0117$
	15-20 nm	18.13 ± 2.55 (18.42)	17.91 ± 4.28 (12.91)	$p = 0.4929$
	20-25 nm	11.79 ± 2.10 (12.31)	14.28 ± 2.73 (16.15)	$p = 0.5104$
	25-30 nm	18.29 ± 3.29 (11.83)	13.74 ± 3.28 (10.44)	$p = 0.3364$
	30-35 nm	15.05 ± 2.57 (16.15)	11.54 ± 2.23 (10.09)	$p = 0.3071$
	35-40 nm	13.1 ± 2.68 (10.56)	12.53 ± 2.45 (12.57)	$p = 0.8623$
	40-80 nm	152.3 ± 13.4 (145.3)	108.4 ± 12.08 (85.71)	$^{*}p = 0.0231$
	80-120 nm	154.0 ± 12.56 (165.8)	92.95 ± 13.17 (77.47)	$^{**}p = 0.0016$
	120-160 nm	153.2 ± 18.75 (130.4)	63.03 ± 8.99 (62.64)	$^{****}p < 0.0001$
	160-200 nm	120.9 ± 16.6 (98.5)	33.19 ± 8.12 (16.15)	$^{****}p < 0.0001$
Diameter (nm)	all SVs	50.62 ± 0.66 (50.37)	50.63 ± 1.03 (49.94)	$p = 0.9924$
	docked SVs	50.29 ± 0.76 (50.28)	46.23 ± 1.03 (47.70)	$^{**}p = 0.0035$
	membrane-proximal SVs	50.72 ± 0.76 (50.22)	50.87 ± 1.09 (49.91)	$p = 0.8194$
Ratio	0-2/0-40 nm	0.1579 ± 0.0239 (0.1250)	0.1203 ± 0.0304 (0.0769)	$p = 0.1713$

Table S5. Quantitative analysis of SV numbers, diameters and the AZ area of 6M wt and *Otof*$^{-/-}$ mice. Related to Figure 2-6.

Distance to AZ membrane	wt P10	wt P21	wt 6M	*p*-value
0-10 nm	73.22 ± 10.10 (67.48)	81.72 ± 14.20 (60.77)	113.1 ± 14.9 (98.9)	$p = 0.1224$
10-20 nm	28.14 ± 5.86 (16.59)	33.64 ± 6.14 (25.03)	49.79 ± 5.42 (46.61)	wt P10 vs. wt P21: $p > 0.9999$ wt P10 vs. wt 6M: $^{**}p = 0.0096$ wt P21 vs. wt 6M: $p = 0.1125$
20-30 nm	30.67 ± 5.37 (24.51)	29.72 ± 5.78 (29.95)	30.08 ± 4.39 (25.55)	$p = 0.9919$
30-40 nm	33.33 ± 4.24 (30.85)	25.69 ± 3.85 (18.83)	28.15 ± 3.74 (29.72)	$p = 0.4074$
40-50 nm	31.67 ± 3.98 (32.44)	34.56 ± 3.89 (33.10)	29.31 ± 3.34 (29.72)	$p = 0.6083$
50-60 nm	25.68 ± 3.48 (23.53)	37.17 ± 6.19 (33.86)	36.93 ± 4.33 (36.93)	$p = 0.1731$
60-70 nm	36.72 ± 6.45 (29.78)	36.93 ± 5.43 (30.25)	40.85 ± 6.58 (34.96)	$p = 0.9404$
70-80 nm	21.00 ± 4.10 (21.93)	33.81 ± 5.76 (28.47)	45.91 ± 6.01 (43.97)	wt P10 vs. wt P21: $p = 0.3456$ wt P10 vs. wt 6M: $^{**}p = 0.0055$ wt P21 vs. wt 6M: $p = 0.4853$
80-90 nm	26.09 ± 4.87 (16.91)	25.35 ± 3.35 (24.20)	44.14 ± 5.57 (38.14)	wt P10 vs. wt P21: $p = 0.9943$ wt P10 vs. wt 6M: $^{*}p = 0.0257$ wt P21 vs. wt 6M: $^{*}p = 0.0230$
90-100 nm	18.01 ± 3.75 (14.77)	33.36 ± 7.30 (21.49)	38.33 ± 4.36 (34.96)	wt P10 vs. wt P21: $p = 0.2205$ wt P10 vs. wt 6M: $^{**}p = 0.0031$ wt P21 vs. wt 6M: $p = 0.5444$
100-110 nm	22.37 ± 3.14 (22.19)	29.31 ± 7.12 (18.64)	35.77 ± 4.39 (32.29)	$p = 0.1557$
110-120 nm	22.63 ± 4.08 (16.66)	26.56 ± 7.10 (15.69)	35.76 ± 4.56 (32.29)	$p = 0.1772$
120-130 nm	19.63 ± 4.03 (13.98)	26.21 ± 6.36 (17.21)	46.32 ± 6.45 (48.44)	wt P10 vs. wt P21: $p > 0.9999$ wt P10 vs. wt 6M: $^{*}p = 0.0132$ wt P21 vs. wt 6M: $p = 0.0973$
130-140 nm	17.81 ± 3.83 (14.49)	23.51 ± 5.16 (16.60)	41.84 ± 6.65 (32.57)	wt P10 vs. wt P21: $p > 0.9999$ wt P10 vs. wt 6M: $^{*}p = 0.0291$ wt P21 vs. wt 6M: $p = 0.2797$
140-150 nm	13.24 ± 3.04 (9.38)	19.21 ± 3.91 (15.49)	31.45 ± 5.25 (25.35)	wt P10 vs. wt P21: $p = 0.6271$ wt P10 vs. wt 6M: $^{**}p = 0.0098$ wt P21 vs. wt 6M: $p = 0.1252$
150-160 nm	17.60 ± 4.33 (11.49)	19.36 ± 5.25 (12.54)	33.55 ± 4.59 (25.43)	wt P10 vs. wt P21: $p > 0.9999$ wt P10 vs. wt 6M: $^{*}p = 0.0260$ wt P21 vs. wt 6M: $p = 0.0730$
160-170 nm	10.60 ± 2.81 (6.07)	22.25 ± 8.47 (9.62)	29.52 ± 4.53 (11.61)	wt P10 vs. wt P21: $p > 0.9999$ wt P10 vs. wt 6M: $^{**}p = 0.0051$ wt P21 vs. wt 6M: $p = 0.0917$
170-180 nm	8.62 ± 2.40 (0.00)	20.30 ± 7.25 (8.07)	36.18 ± 5.47 (26.68)	wt P10 vs. wt P21: $p = 0.9048$ wt P10 vs. wt 6M: $^{***}p = 0.0004$

				wt P21 vs. wt 6M: **p* = 0.0227
180-190 nm	10.88 ± 2.46 (9.32)	20.72 ± 6.40 (8.39)	27.91 ± 5.22 (20.86)	p = 0.0737
190-200 nm	9.52 ± 2.88 (0.00)	14.82 ± 5.71 (6.91)	27.28 ± 4.82 (19.75)	wt P10 vs. wt P21: *p* > 0.9999 wt P10 vs. wt 6M: **p* = 0.0144 wt P21 vs. wt 6M: *p* = 0.0875

Table S6. SV distribution at wt AZs, Related to Figure S1 and Figure 2 showing the number of SVs within bins of 10 nm from the AZ membrane normalized to the AZ area.

Distance to AZ membrane	***Otof*$^{-/-}$ P10**	***Otof*$^{-/-}$ P22**	***Otof*$^{-/-}$ 6M**	***p*-value**
0-10 nm	54.63 ± 11.57 (38.18)	61.04 ± 12.13 (53.58)	53.13 ± 9.27 (49.55)	*p* = 0.9168
10-20 nm	27.10 ± 4.13 (30.15)	48.86 ± 9.60 (40.27)	35.93 ± 6.35 (28.40)	*p* = 0.3884
20-30 nm	18.01 ± 4.17 (13.03)	17.70 ± 3.23 (16.37)	31.66 ± 3.85 (28.60)	ANOVA: *p* = 0.0486 Tukey's: *Otof*$^{-/-}$ P10 vs. *Otof*$^{-/-}$ P21: *p* = 0.1092 *Otof*$^{-/-}$ P10 vs. *Otof*$^{-/-}$ 6M: *p* = 0.9753 *Otof*$^{-/-}$ P21 vs. *Otof*$^{-/-}$ 6M: *p* = 0.0649
30-40 nm	27.42 ± 4.08 (22.96)	29.50 ± 4.32 (24.42)	24.07 ± 3.47 (24.23)	*p* = 0.6192
40-50 nm	31.69 ± 5.89 (30.31)	34.70 ± 5.03 (35.79)	27.00 ± 4.06 (25.14)	*p* = 0.5494
50-60 nm	30.98 ± 5.26 (31.92)	43.47 ± 6.20 (38.76)	29.77 ± 5.03 (25.82)	*p* = 0.1582
60-70 nm	35.39 ± 7.09 (26.36)	38.54 ± 4.32 (32.15)	24.53 ± 3.93 (20.36)	*p* = 0.1453
70-80 nm	31.03 ± 5.55 (23.72)	42.23 ± 6.80 (36.63)	27.10 ± 4.71 (21.43)	*p* = 0.1604
80-90 nm	33.69 ± 6.15 (22.13)	34.26 ± 6.50 (32.32)	23.63 ± 5.20 (17.90)	*p* = 0.3314
90-100 nm	30.03 ± 6.51 (19.57)	39.63 ± 6.50 (32.77)	24.79 ± 3.39 (26.90)	*p* = 0.1719
100-110 nm	31.65 ± 6.24 (23.74)	41.47 ± 6.10 (32.17)	23.94 ± 4.36 (19.82)	*p* = 0.0914
110-120 nm	27.12 ± 4.60 (22.22)	41.20 ± 9.15 (31.43)	20.58 ± 3.94 (19.82)	*p* = 0.0703
120-130 nm	26.96 ± 6.49 (16.36)	33.81 ± 5.98 (29.91)	17.92 ± 3.37 (17.52)	*p* = 0.1197
130-140 nm	31.52 ± 6.87 (15.85)	32.56 ± 6.89 (22.80)	15.94 ± 3.14 (16.15)	*p* = 0.0871
140-150 nm	26.63 ± 5.96 (19.67)	30.08 ± 6.43 (26.69)	16.54 ± 3.53 (12.51)	*p* = 0.3041
150-160 nm	20.94 ± 4.01 (20.16)	28.48 ± 5.02 (22.80)	12.63 ± 3.35 (8.08)	*Otof*$^{-/-}$ P10 vs. *Otof*$^{-/-}$ P21: *p* = 0.4186 *Otof*$^{-/-}$ P10 vs. *Otof*$^{-/-}$ 6M: *p* = 0.3474 *Otof*$^{-/-}$ P21 vs. *Otof*$^{-/-}$ 6M: **p* = 0.0239
160-170 nm	25.07 ± 5.94 (16.22)	30.75 ± 7.09 (18.17)	11.00 ± 3.00 (6.63)	KW: *p* = 0.0487 Dunn's: *Otof*$^{-/-}$ P10 vs. *Otof*$^{-/-}$ P21: *p* > 0.9999 *Otof*$^{-/-}$ P10 vs. *Otof*$^{-/-}$ 6M: *p* = 0.2484 *Otof*$^{-/-}$ P21 vs. *Otof*$^{-/-}$ 6M: *p* = 0.0519

170-180 nm	26.18 ± 5.53 (19.67)	24.78 ± 4.95 (18.86)	11.46 ± 3.19 (0.00)	KW: $p = 0.0475$ Dunn's: *Otof*$^{-/-}$ P10 vs. *Otof*$^{-/-}$ P21: $p > 0.9999$ *Otof*$^{-/-}$ P10 vs. *Otof*$^{-/-}$ 6M: $p = 0.0871$ *Otof*$^{-/-}$ P21 vs. *Otof*$^{-/-}$ 6M: $p = 0.1089$
180-190 nm	14.93 ± 4.49 (7.04)	15.89 ± 4.54 (10.10)	4.98 ± 1.68 (0.00)	$p = 0.1300$
190-200 nm	16.97 ± 3.83 (11.24)	20.89 ± 5.67 (12.04)	5.74 ± 1.84 (0.00)	*Otof*$^{-/-}$ P10 vs. *Otof*$^{-/-}$ P21: $p > 0.9999$ *Otof*$^{-/-}$ P10 vs. *Otof*$^{-/-}$ 6M: $*p = 0.0494$ *Otof*$^{-/-}$ P21 vs. *Otof*$^{-/-}$ 6M: $p = 0.0716$

Table S7. SV distribution at *Otof*$^{-/-}$ AZs, Related to Figure S1 and Figure 2 showing the number of SVs within bins of 10 nm from the AZ membrane normalized to the AZ area.

Distance to AZ membrane	wt P10	*Otof*$^{-/-}$ P10	*p*-value
0-10 nm	73.22 ± 10.10 (67.48)	54.63 ± 11.57 (38.18)	*p* = 0.1089
10-20 nm	28.14 ± 5.86 (16.59)	27.10 ± 4.13 (30.15)	*p* = 0.7771
20-30 nm	30.67 ± 5.37 (24.51)	18.01 ± 4.17 (13.03)	*p* = 0.8875
30-40 nm	33.33 ± 4.24 (30.85)	27.42 ± 4.08 (22.96)	*p* = 0.2205
40-50 nm	31.67 ± 3.98 (32.44)	31.69 ± 5.89 (30.31)	*p* = 0.7112
50-60 nm	25.68 ± 3.48 (23.53)	30.98 ± 5.26 (31.92)	*p* = 0.4056
60-70 nm	36.72 ± 6.45 (29.78)	35.39 ± 7.09 (26.36)	*p* = 0.7439
70-80 nm	21.00 ± 4.10 (21.93)	31.03 ± 5.55 (23.72)	*p* = 0.1965
80-90 nm	26.09 ± 4.87 (16.91)	33.69 ± 6.15 (22.13)	*p* = 0.3379
90-100 nm	18.01 ± 3.75 (14.77)	30.03 ± 6.51 (19.57)	*p* = 0.2842
100-110 nm	22.37 ± 3.14 (22.19)	31.65 ± 6.24 (23.74)	*p* = 0.5416
110-120 nm	22.63 ± 4.08 (16.66)	27.12 ± 4.60 (22.22)	*p* = 0.4688
120-130 nm	19.63 ± 4.03 (13.98)	26.96 ± 6.49 (16.36)	*p* = 0.7604
130-140 nm	17.81 ± 3.83 (14.49)	31.52 ± 6.87 (15.85)	*p* = 0.1709
140-150 nm	13.24 ± 3.04 (9.38)	26.63 ± 5.96 (19.67)	*p* = 0.1089
150-160 nm	17.60 ± 4.33 (11.49)	20.94 ± 4.01 (20.16)	*p* = 0.4008
160-170 nm	10.60 ± 2.81 (6.07)	25.07 ± 5.94 (16.22)	*p* = 0.1065
170-180 nm	8.62 ± 2.40 (0.00)	26.18 ± 5.53 (19.67)	**p* = 0.0141
180-190 nm	10.88 ± 2.46 (9.32)	14.93 ± 4.49 (7.04)	*p* = 0.9479
190-200 nm	9.52 ± 2.88 (0.00)	16.97 ± 3.83 (11.24)	**p* = 0.0497

Table S8. SV distribution at P10 wt and *Otof*$^{-/-}$ AZs, Related to Figure S1 and Figure 2 showing the number of SVs within bins of 10 nm from the AZ membrane normalized to the AZ area.

Distance to AZ membrane	wt P21	*Otof*$^{-/-}$ P22	*p*-value
0-10 nm	81.72 ± 14.20 (60.77)	61.04 ± 12.13 (53.58)	*p* = 0.2140
10-20 nm	33,64 ± 6.14 (25.03)	48.86 ± 9.60 (40.27)	*p* = 0.4174
20-30 nm	29.72 ± 5.78 (29.95)	17.70 ± 3.23 (16.37)	**p* = 0.0221
30-40 nm	25.69 ± 3.85 (18.83)	29.50 ± 4.32 (24.42)	*p* = 0.5067
40-50 nm	34.56 ± 3.89 (33.10)	34.70 ± 5.03 (35.79)	*p* = 0.9831
50-60 nm	37.17 ± 6.19 (33.86)	43.47 ± 6.20 (38.76)	*p* = 0.5435
60-70 nm	36.93 ± 5.43 (30.25)	38.54 ± 4.32 (32.15)	*p* = 0.8177
70-80 nm	33.81 ± 5.76 (28.47)	42.23 ± 6.80 (36.63)	*p* = 0.3554
80-90 nm	25.35 ± 3.35 (24.20)	34.26 ± 6.50 (32.32)	*p* = 0.3437
90-100 nm	33.36 ± 7.30 (21.49)	39.63 ± 6.50 (32.77)	*p* = 0.4174
100-110 nm	29.31 ± 7.12 (18.64)	41.47 ± 6.10 (32.17)	*p* = 0.0977
110-120 nm	26.56 ± 7.10 (15.69)	41.20 ± 9.15 (31.43)	*p* = 0.2313
120-130 nm	26.21 ± 6.36 (17.21)	33.81 ± 5.98 (29.91)	*p* = 0.2140
130-140 nm	23.51 ± 5.16 (16.60)	32.56 ± 6.89 (22.80)	*p* = 0.4712
140-150 nm	19.21 ± 3.91 (15.49)	30.08 ± 6.43 (26.69)	*p* = 0.3673
150-160 nm	19.36 ± 5.25 (12.54)	28.48 ± 5.02 (22.80)	*p* = 0.1822
160-170 nm	22.25 ± 8.47 (9.62)	30.75 ± 7.09 (18.17)	*p* = 0.1025
170-180 nm	20.30 ± 7.25 (8.07)	24.78 ± 4.95 (18.86)	*p* = 0.1411
180-190 nm	20.72 ± 6.40 (8.39)	15.89 ± 4.54 (10.10)	*p* = 0.7359
190-200 nm	14.82 ± 5.71 (6.91)	20.89 ± 5.67 (12.04)	*p* = 0.3919

Table S9. SV distribution at P21/22 wt and *Otof*$^{-/-}$ AZs, Related to Figure S1 and Figure 2 showing the number of SVs within bins of 10 nm from the AZ membrane normalized to the AZ area.

Distance to AZ membrane	wt 6M	*Otof*$^{-/-}$ 6M	*p*-value
0-10 nm	113.1 ± 14.9 (98.9)	53.13 ± 9.27 (49.55)	***p* = 0.0016
10-20 nm	49.79 ± 5.42 (46.61)	35.93 ± 6.35 (28.40)	*p* = 0.0598
20-30 nm	30.08 ± 4.39 (25.55)	31.66 ± 3.85 (28.60)	*p* = 0.6413
30-40 nm	28.15 ± 3.74 (29.72)	24.07 ± 3.47 (24.23)	*p* = 0.4280
40-50 nm	29.31 ± 3.34 (29.72)	27.00 ± 4.06 (25.14)	*p* = 0.6628
50-60 nm	36.93 ± 4.33 (36.93)	29.77 ± 5.03 (25.82)	*p* = 0.3320
60-70 nm	40.85 ± 6.58 (34.96)	24.53 ± 3.93 (20.36)	*p* = 0.0753
70-80 nm	45.91 ± 6.01 (43.97)	27.10 ± 4.71 (21.43)	**p* = 0.0288
80-90 nm	44.14 ± 5.57 (38.14)	23.63 ± 5.20 (17.90)	***p* = 0.0038
90-100 nm	38.33 ± 4.36 (34.96)	24.79 ± 3.39 (26.90)	**p* = 0.0179
100-110 nm	35.77 ± 4.39 (32.29)	23.94 ± 4.36 (19.82)	*p* = 0.0617
110-120 nm	35.76 ± 4.56 (32.29)	20.58 ± 3.94 (19.82)	**p* = 0.0150
120-130 nm	46.32 ± 6.45 (48.44)	17.92 ± 3.37 (17.52)	****p* = 0.0003
130-140 nm	41.84 ± 6.65 (32.57)	15.94 ± 3.14 (16.15)	***p* = 0.0011
140-150 nm	31.45 ± 5.25 (25.35)	16.54 ± 3.53 (12.51)	**p* = 0.0226
150-160 nm	33.55 ± 4.59 (25.43)	12.63 ± 3.35 (8.08)	****p* = 0.0009
160-170 nm	29.52 ± 4.53 (11.61)	11.00 ± 3.00 (6.63)	***p* = 0.0032
170-180 nm	36.18 ± 5.47 (26.68)	11.46 ± 3.19 (0.00)	****p* = 0.0006
180-190 nm	27.91 ± 5.22 (20.86)	4.98 ± 1.68 (0.00)	****p* = 0.0004
190-200 nm	27.28 ± 4.82 (19.75)	5.74 ± 1.84 (0.00)	***p* = 0.0011

Table S10. SV distribution at 6M wt and *Otof*$^{-/-}$ AZs, Related to Figure S1 and Figure 2 showing the number of SVs within bins of 10 nm from the AZ membrane normalized to the AZ area.

Docked SVs	**Adjusted *p*-value**
wt P10 vs. wt P21	$p = 0.6397$
wt P10 vs. wt 6M	$p = 0.4507$
wt P21 vs. wt 6M	$p = 0.7755$
Otof$^{-/-}$ P10 vs. *Otof*$^{-/-}$ P22	$p = 0.0809$
Otof$^{-/-}$ P10 vs. *Otof*$^{-/-}$ 6M	$p = 0.4507$
Otof$^{-/-}$ P22 vs. *Otof*$^{-/-}$6M	$p = 0.2475$
wt P10 vs. *Otof*$^{-/-}$ P10	$p = 0.2475$
wt P21 vs. *Otof*$^{-/-}$ P22	$p = 0.4232$
wt 6M vs. *Otof*$^{-/-}$ 6M	$p = 0.8987$
Membrane-proximal SVs	
wt P10 vs. wt P21	$p = 0.7749$
wt P10 vs. wt 6M	$p = 0.9717$
wt P21 vs. wt 6M	$p = 0.7297$
Otof$^{-/-}$ P10 vs. *Otof*$^{-/-}$ P22	$*p = 0.0300$
Otof$^{-/-}$ P10 vs. *Otof*$^{-/-}$ 6M	$p = 0.9717$
Otof$^{-/-}$ P22 vs. *Otof*$^{-/-}$6M	$*p = 0.0300$
wt P10 vs. *Otof*$^{-/-}$ P10	$p = 0.5343$
wt P21 vs. *Otof*$^{-/-}$ P22	$p = 0.3084$
wt 6M vs. *Otof*$^{-/-}$ 6M	$p = 0.5343$

Table S11. Comparison of the number of docked and membrane-proximal SVs, Related to Figure 4,5.

Transparent Methods

Animals

C57BL6/J (wild-type, wt) and otoferlin knockout (*Otof*$^{-/-}$) mice in a C57BL6/N background (Reisinger et al., 2011) at postnatal day (P) 10, and P21/22 as well as six-month-old animals (6M) of either sex were used for this study. Mice were housed in groups in individually ventilated cage racks with ad libitum access to food and water. All experiments were performed in compliance with the national animal care guidelines, and were approved by the animal welfare of the University of Göttingen and the State of Lower Saxony.

Vibratome slice Preparation

Parasagittal slices (150 µm) of CN were prepared as described previously (Butola et al., 2017; Mendoza Schulz et al., 2014; Yang & Xu-Friedman, 2008). Brains were dissected and immersed in ice-cold cutting solution containing (in mM) 50 NaCl, 26 $NaHCO_3$, 120 sucrose, 1.25 $NaH_2PO_4xH_2O$, 2.5 KCl, 20 glucose, 0.2 $CaCl_2$, 6 $MgCl_2$, 0.7 Na L-ascorbate, 2 Na pyruvate, 3 myo-inositol, and 3 Na L-lactate with an osmolarity of around 310 mOsm, pH adjusted to 7.35, continuously aerated with carbogen (95% O_2, 5% CO_2). The meninges were removed from the ventral part of the brainstem, and hemispheres were separated by a midsagital cut. Then the forebrain was removed at the pons-midbrain junction. Brain blocks containing the brainstem and the cerebellum were glued onto the specimen plate of a VT 1200 S vibratome (Leica microsystems, Wetzlar, Germany) with the lateral sides facing upwards and the ventral side facing the blade. The specimen plate was then transferred to the buffer tray containing ice-cold cutting solution.

Sections were cut at a blade feed rate of 0.02 mm/s with an amplitude of 1.50 mm. Slices containing the AVCN were trimmed and prepared for high-pressure freezing.

High-pressure freezing

The slices of the AVCN were mounted onto type A specimen carriers (Leica Microsystems, Wetzlar, Germany) with a diameter of 3 mm and a depth of 0.2 mm, filled with cutting solution. The flat side of the type B carriers (Leica Microsystems, Wetzlar, Germany) was dipped in 1-hexadecene (Sigma-Aldrich, Wetzlar, Germany) and placed onto the type A carrier. Samples were frozen immediately using a HPM100 (Leica Microsystems, Wetzlar, Germany) and transferred into liquid nitrogen for storage or further processing.

Freeze-substitution

Freeze-substitution was performed in an EM AFS2 (Leica Microsystems, Wetzlar, Germany) as described previously (Chakrabarti et al., 2018; Wong et al., 2014). The slices were incubated in 0.1% (w/v) tannic acid in acetone at −90°C for 4 days and afterward washed three times for 1 h each in acetone at −90°C. 2% (w/v) osmium tetroxide in acetone was applied and incubated for 40.4 h. The temperature maintained at −90°C for 7 h, before it rose to -20°C within another 14 h (5°C/h). Over a period of 14.5 h the temperature further rose to 4°C (10°C/h). At 4°C, osmium tetroxide was removed, and the samples were washed with acetone three times and brought to room temperature. Slices were infiltrated in epoxy resin (Agar-100 kit, Plano, Germany; epoxy/acetone 1:1 3-6 h; 100% epoxy resin overnight). Finally, samples were further incubated in fresh 100% epoxy resin end placed in embedding molds.

Ultrathin-sectioning and post-staining

After polymerization for 48 h at 70°C, excess resin was removed with a fine file (DiAtome, Switzerland) and the block was trimmed to a pyramid using a razor blade. To check the region and the structural preservation, 70 nm ultrathin sections were cut with a diamond knife (DiAtome, Switzerland) using an EM UC7 (Leica Microsystems, Wetzlar, Germany) ultramicrotome. Sections were collected on formvar-coated copper slot grids (slot; Athene, Plano, Wetzlar, Germany). For electron tomography, 250 nm semi-thin sections were obtained and collected on formvar-covered mesh grids (100 mesh; Athene, Plano, Wetzlar, Germany). Poststaining was performed with UranyLess (EMS, Hatfield, PA) for 20 minutes.

Transmission electron microscopy and electron tomography

To check the quality of the tissue, 2D electron micrographs were taken at 80 kV using a JEM1011 transmission electron microscope (JEOL, Freising, Germany) equipped with a Gatan Orius 1200A camera (Gatan, Munich, Germany). For each animal, tomograms were acquired from two different AVCN vibratome slices. At least 5-10 grids with approx. 5 sections were cut consecutively for each vibratome slice. In total approx. 20 grids per animal were cut. The tomograms were taken from different grids and within one grid from different regions.

After prescreening of the grids, endbulb of Held active zones (AZs) of the AVCN were chosen by the appearance of a large presynaptic terminal contacting the principal cell with an asymmetric (denoted as postsynaptic density (PSD)) synaptic site.

Electron tomography was performed as described previously (Chakrabarti et al., 2018; Wong et al., 2014). 10 nm gold beads (British Bio Cell/Plano, Germany) were applied to both sides of the stained grids. Big synaptic terminals on bushy cells were identified and tilt series from endbulb AZs were acquired at 200 kV using a JEM2100 transmission electron microscope (JEOL, Freising, Germany) mostly from −60° to +60° with a 1° increment at 15,000× using the Serial-EM software package (Mastronarde, 2005). Tomograms were generated using the IMOD package etomo (Kremer et al., 1996).

Model rendering and image analysis

In high-pressure frozen samples, PSDs appear less electron-dense compared to chemical fixed synapses. Thus, only asymmetric synapses with a clearly visible synaptic cleft at 0° and a clearly identifiable PSD were analyzed. Moreover, just tomograms of AZs within big synaptic terminals that are typical for endbulbs of Held were generated.

Tomograms were segmented semi-automatically using 3dmod (Kremer et al., 1996), with a pixel size of 0.95 nm. The presynaptic AZ membrane was defined as part of the presynaptic membrane that was opposed to the PSD and the PSD was determined along a clear synaptic cleft. Previous studies did comparable approaches on conventionally embedded endbulbs of Held (Butola et al., 2017) as well as calyces of Held (Taschenberger et al., 2002), demonstrating that the measurement of the membrane along the PSD extent is a valid approximation for the presynaptic AZ size. The AZ membrane of an AZ was then assigned as a closed object and manually segmented every 15 virtual sections for 5 consecutive virtual sections and then interpolated across the Z-stack. The total surface area of this object was then divided by two to calculate the presynaptic AZ area.

SVs were reconstructed using a spherical “scattered” object at its maximum projection and the sphere size was adjusted for each vesicle. The number of SVs was presented as total number per AZ as well as normalized to the size of the AZ area. The smallest distances from the outer leaflet of the SV membrane to the inner leaflet of the AZ membrane were measured and SVs in physical contact with the AZ membrane were defined as morphological docked SVs (0-2 nm distance). All SVs within 200 nm perpendicular to the AZ membrane were quantified in 5 nm bins up to 40 nm, and in 40 nm bins (40-80 nm; 80-120 nm; 120-160 nm; 160-200 nm). Additionally, 10 nm bins were applied across the entire range of 0-200 nm. The number of SVs in the respective bins was normalized to the AZ area. The radii of the SVs were determined with the program “imodinfo” of the IMOD software package and the average diameter per tomogram was calculated.

Statistical analysis

The sample size analyzed in this study was as following: wt P10: *N* = 4 mice, *n* = 24 AZs (=tomograms); P21: *N* = 3 mice, *n* = 22 AZs; 6M: *N* = 3 mice, *n* = 29 AZs *Otof*$^{-/-}$ P10: *N* = 3 mice, *n* = 22 AZs; P22: *N* = 3 mice, *n* = 23 AZs; 6M: *N* = 3 mice, *n* = 23 AZs.

For SV analysis:

All SVs: wt P10 (*N* = 4; *n* = 1101), *Otof*$^{-/-}$ P10 (*N* = 3; *n* = 1078), wt P21 (*N* = 3; *n* = 1190), *Otof*$^{-/-}$ P22 (*N* = 3; *n* = 1508), wt 6M (*N* = 3; *n* = 1842) and *Otof*$^{-/-}$ 6M (*N* = 3; *n* = 911), (*N*, number of animals; *n*, number of SVs).

Docked SVs: wt P10 (*N* = 4; *n* = 85), *Otof*$^{-/-}$ P10 (*N* = 3; *n* = 60), wt P21 (*N* = 3; *n* = 67), *Otof*$^{-/-}$ P22 (*N* = 3; *n* = 56), wt 6M (*N* = 3; *n* = 86) and *Otof*$^{-/-}$ 6M (*N* = 3; *n* = 42), (*N*, number of animals; *n*, number of SVs).

Membrane-proximal SVs: wt P10 (*N* = 4; *n* = 292), *Otof*$^{-/-}$ P10 (*N* = 3; *n* = 195), wt P21 (*N* = 3; *n* = 283), *Otof*$^{-/-}$ P22 (*N* = 3; *n* = 354), wt 6M (*N* = 3; *n* = 420) and *Otof*$^{-/-}$ 6M (*N* = 3; *n* = 248), (*N*, number of animals; *n*, number of SVs).

Data were analyzed using *Excel*, *Igor Pro 7* (Wavemetrics) *GraphPad Prism 8* (GraphPad Software) and *R* version 4.0.3. Normal distribution was assessed with the Jarque-Bera test and equality of variances was assessed with the *F*-test in normally distributed data*. Data from wt and Otof*$^{-/-}$ *were compared for each age group by* two-sample tests*.* For normally distributed, two-tailed unpaired *t*-test, or, when not normally distributed, the Wilcoxon rank test was used. *In addition, the different age groups were compared separately for wt and Otof*$^{-/-}$*.* One-way ANOVA with post-hoc correction by Tukey’s test was used to detect differences for normally distributed data. For not normally distributed data Kruskal–Wallis (KW) test followed by Dunn’s test was used. For analyzing SV diameters in Fig. 6A,C,E, the mean of the averaged SV diameters per tomogram were compared. To compare variances in Fig. 4 and 5, *F*-test was used and the

corresponding *p*-values were corrected for multiple comparisons. Statistically significant differences are reported as *$p < 0.05$, **$p < 0.01$, ***$p < 0.001$ and ****$p < 0.0001$.

Supplemental References

Butola, T., Wichmann, C., & Moser, T. (2017). Piccolo Promotes Vesicle Replenishment at a Fast Central Auditory Synapse. *Frontiers in Synaptic Neuroscience*, *9*, 14. https://doi.org/10.3389/fnsyn.2017.00014

Chakrabarti, R., Michanski, S., & Wichmann, C. (2018). Vesicle sub-pool organization at inner hair cell ribbon synapses. *EMBO Reports*, e44937. https://doi.org/10.15252/embr.201744937

Kremer, J. R., Mastronarde, D. N., & McIntosh, J. R. (1996). Computer visualization of three-dimensional image data using IMOD. *Journal of Structural Biology*, *116*(1), 71–76. https://doi.org/10.1006/jsbi.1996.0013

Mastronarde, D. N. (2005). Automated electron microscope tomography using robust prediction of specimen movements. *Journal of Structural Biology*, *152*(1), 36–51. https://doi.org/10.1016/j.jsb.2005.07.007

Mendoza Schulz, A., Jing, Z., Sánchez Caro, J. M., Wetzel, F., Dresbach, T., Strenzke, N., Wichmann, C., & Moser, T. (2014). Bassoon-disruption slows vesicle replenishment and induces homeostatic plasticity at a CNS synapse. *The EMBO Journal*, *33*(5), 512–527. https://doi.org/10.1002/embj.201385887

Reisinger, E., Bresee, C., Neef, J., Nair, R., Reuter, K., Bulankina, A., Nouvian, R., Koch, M., Bückers, J., Kastrup, L., Roux, I., Petit, C., Hell, S. W., Brose, N., Rhee, J.-S., Kügler, S., Brigande, J. V., & Moser, T. (2011). Probing the functional equivalence of otoferlin and synaptotagmin 1 in exocytosis. *Journal of Neuroscience*, *31*(13), 4886–4895. https://doi.org/10.1523/JNEUROSCI.5122-10.2011

Wong, A. B., Rutherford, M. A., Gabrielaitis, M., Pangršič, T., Göttfert, F., Frank, T., Michanski, S., Hell, S., Wolf, F., Wichmann, C., & Moser, T. (2014). Developmental refinement of hair cell synapses tightens the coupling of Ca2+ influx to exocytosis. *The EMBO Journal*, *33*(3), 247–264. https://doi.org/10.1002/embj.201387110

Yang, H., & Xu-Friedman, M. A. (2008). Relative roles of different mechanisms of depression at the mouse endbulb of Held. *Journal of Neurophysiology*, *99*(5), 2510–2521. https://doi.org/10.1152/jn.01293.2007